

# Synthesis and Catalytic Evaluation of Silver@nickel Oxide and Alginate Biopolymer Nanocomposite Hydrogel Beads

Ashi Khalil

Institute of Chemical Sciences, University of Peshawar

Nauman Ali (✉ [nali75pk@uop.edu.pk](mailto:nali75pk@uop.edu.pk))

University of Peshawar <https://orcid.org/0000-0002-7485-6843>

Abdullah M. Asiri

Chemistry Department, King Abdul Aziz University, Saudi Arabia

Tahseen Kamal

Centre of Excellence for Advance Material Research, Saudi Arabia

---

## Research Article

**Keywords:** Alginate biopolymer, beads, nanocomposite, reduction, pollutants

**Posted Date:** March 23rd, 2021

**DOI:** <https://doi.org/10.21203/rs.3.rs-314036/v1>

**License:**  This work is licensed under a Creative Commons Attribution 4.0 International License.

[Read Full License](#)

---

**Version of Record:** A version of this preprint was published at Cellulose on October 18th, 2021. See the published version at <https://doi.org/10.1007/s10570-021-04248-0>.

1   **Synthesis and catalytic evaluation of silver@nickel oxide and alginate**  
2   **biopolymer nanocomposite hydrogel beads**

3                  Ashi Khalil<sup>a</sup>, Nauman Ali <sup>a\*</sup>, Abdullah M. Asiri <sup>bc</sup>, Tahseen Kamal <sup>c</sup>

4

5

6

7   *<sup>a</sup>Institute of Chemical Sciences, University of Peshawar, Pakistan*

8   *<sup>b</sup>Chemistry Department, Faculty of Science, King Abdulaziz University, P. O. Box 80203, Jeddah  
9   21589, Saudi Arabia.*

10   *<sup>c</sup>Center of Excellence for Advanced Materials Research, King Abdulaziz University, P. O. Box  
11   80203, Jeddah 21589, Saudi Arabia.*

12

13

14

15

16

17

18

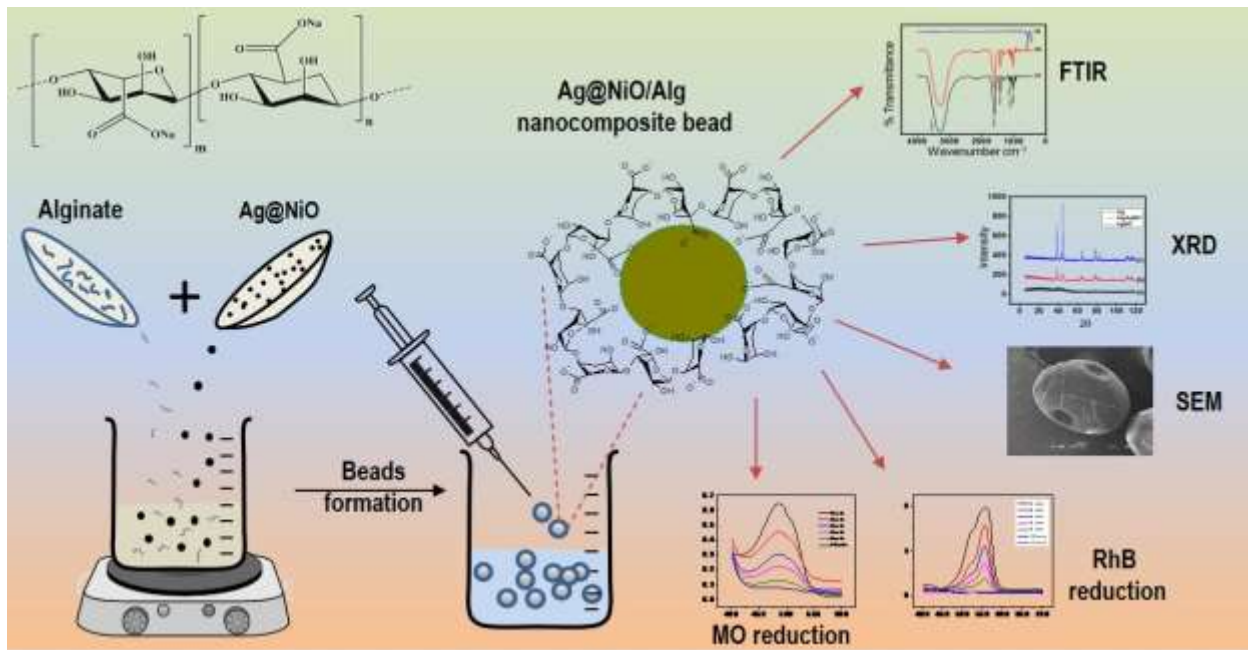
19

20

21   \*Correspondence should be addressed to Dr. Nauman Ali; nali75pk@uop.edu.pk

22

23 **Graphical abstract**



24  
25 **Abstract**

In this study, silver-nickel oxide/ calcium alginate ( $\text{Ag@NiO/Alg}$ ) hydrogel beads were synthesized. The preparation of  $\text{Ag@NiO}$  was carried out in two steps: 1) synthesizing the nickel oxide nanoparticle through precipitation method, and 2) adhering of the  $\text{Ag}^+$  ion from silver nitrate solution and reduction with sodium borohydride. The nanomaterial was mixed with alginate biopolymer aqueous solution and extruded through syringe in a dropwise manner into a  $\text{CaCl}_2$  aqueous solution for inotropic crosslinking. Through this method,  $\text{Ag@NiO/Alg}$  beads were formed which were characterized by different instrumental techniques. The catalytic efficiency of  $\text{Ag@NiO/Alg}$  was evaluated for the reduction of rhodamine B (RhB) and methyl orange (MO), in the presence of sodium borohydride reducing agent. The uncatalyzed RhB and MO reduction reactions did not show a significant decrease in the absorbance value at  $\lambda_{\max}$  within the given experimental time. It was due to the large kinetic barrier. A small decrease in the absorbance value for uncatalyzed reaction in the presence of very high concentration of

38 reducing agent was observed, indicating that the reactions are thermodynamically feasible. After  
39 applying various kinetic order equations to the experimental data, the reactions were found to  
40 follow *pseudo-first order* kinetics using the Ag@NiO/Alg catalyst. The apparent rate constants  
41 ( $k_{app}$ ) were determined as  $0.33358 \text{ min}^{-1}$  and  $0.20882 \text{ min}^{-1}$  for catalytic reduction of RhB and  
42 MO, respectively. Furthermore, reduction reactions were studied at varying dye concentration  
43 and catalyst dosages. The recovered catalyst was reused up to five cycles without significant  
44 drop in the activity.

45 **Keywords:** Alginate biopolymer; beads; nanocomposite; reduction; pollutants

46    **Introduction**

47    Hydrogels with 3-D interwoven structure and high-water retention capacity has found much  
48    attention among various researchers' groups(Khan et al. 2020; Al-Ghamdi and Khan 2020).  
49    Biopolymer based hydrogels have introduced a new thought of green and sustainable catalytic  
50    system. The intermolecular attractive forces (such as covalent bonding, hydrogen bonding etc)  
51    between the polymer chains are held responsible for the uniform immobilization of metallic  
52    nanoparticles inside the polymeric matrix(Khan et al. 2016a, b). Hydrophilic nature of the  
53    hydrogels renders quasi-homogeneous properties to the nanoparticles, hence, enhancing its  
54    catalytic efficiency. Different biopolymer-based hydrogels such as carboxy methyl cellulose;  
55    chitosan, agar, bacterial cellulose, and alginate etc. have been studied so far for academically and  
56    applied in various applied fields (Chen et al. 2017a; Ali et al. 2017a, b, c; Xu et al. 2017b; Silva  
57    et al. 2019; Chanthiwong et al. 2020; Khalil et al. 2020). Amongst them alginate is one of the  
58    most extensively used polymers owing to its highly biocompatible and biodegradable nature. For  
59    instance, Gan *et al* utilized sodium alginate hydrogel beads as a support for graphene oxide and  
60    investigated its catalytic activity for removal of organic dyes and bisphenol A in aqueous  
61    solution (Gan et al. 2018). Lam *et al* utilized TiO<sub>2</sub> nanoparticles immobilized in calcium alginate  
62    beads for photocatalytic degradation of methylene blue (Lam et al. 2017). The chemical structure  
63    of alginate consists of covalently bonded 1,4-linked  $\alpha$ -l-guluronic acids (G) and  $\beta$ -D-mannuronic  
64    acids (M) as main constituents. Unlike other biopolymers which require toxic organic  
65    crosslinking agents, alginates can be ionotropically crosslinked. Owed by the presence of  
66    divalent cations (e.g., Ca<sup>2+</sup>), ionic bridges are formed between the adjacent alginate chains which  
67    lead to its transformation into hydrogel beads in the aqueous medium (Asadi et al. 2018).

68    Metal nanoparticles with particle size in the range of nanometers, exhibiting excellent

69 mechanical and optic-electric properties, have found applications in heterogeneous catalysis.  
70 Various semiconductor metal oxides and noble metals have been studied for its applications as  
71 an efficient catalyst. Recent studies emphasize on the immobilization of noble metals (such as  
72 Ag, Au, Pt and Pd) onto the surface of semiconductor metal oxides ( such as NiO, CuO etc) for  
73 considerable enhancement in its catalytic activity (Kao et al. 2017; Xu et al. 2017a; Chen et al.  
74 2017b; Jiang et al. 2019). Noble metal nanoparticles act as an electron sink for the electron  
75 generated in the semiconductor. Due to excellent optical and catalytic properties of Ag among  
76 the various noble metals, it remains pre-dominant over others. Up-to-date different approaches  
77 have been put forward for the synthesis of AgNiO nanocomposites and studied for its application  
78 in photocatalysis, energy storage, sensors and supercapacitors etc. (Ngo et al. 2017; Nagamuthu  
79 and Ryu 2019; Karimi-Maleh et al. 2020). For instance, Karanmoorthy *et al* reported synthesis of  
80 AgNiO nanocomposite via hydrothermal approach and studied its applications as photocatalyst  
81 for degradation of organic pollutants (Karunamoorthy and Velluchamy 2018). Haq *et al*  
82 investigated green synthesis of Ag/NiO and studied its catalytic efficiency for photodegradation  
83 of organic pollutant rhodamine B (Atta-ul-Haq et al. 2019). Bagtache *et al* synthesized AgNiO  
84 by nitrate route and studied its photoactivity in hydrogen evolution reactions under visible light  
85 (Bagtache et al. 2019). Until now, AgNiO is not yet reported for its application in catalytic  
86 reduction of organic pollutants. Moreover, the employment of a catalyst embedding in a  
87 hydrogel host instead of using the dispersed form of the nanoparticles is beneficial as the catalyst  
88 could be easily recovered for reusing purpose. Therefore, an alginate based biopolymer was  
89 chosen as it could be ionically crosslinked without needing an environmentally toxic agent.  
90 Dyes are widely used for a number of applications in various industries such as textile, dyeing,  
91 plastic, pharmaceutical and many others. These organic dyes, when discharged into the running

92 water in untreated form causes water pollution due to their highly stable and non-biodegradable  
93 nature. They cause severe damage to the aquatic life and may also cause severe health disorders  
94 in human beings. Different physical, chemical and biological methods have been employed for  
95 the removal of these toxic organic pollutants such as adsorption, coagulation, reverse osmosis,  
96 ultrafiltration, biodegradation, oxidation, reduction etc (Kamal et al. 2015; Katheresan et al.  
97 2018; Jamee and Siddique 2019). Amongst them catalytic reduction is considered as primary  
98 choice, owing to less time required for removal of organic pollutants. In addition, the reduction  
99 products obtained as a result of this process have found numerous applications in different fields  
100 (Kamal et al. 2016, 2019; Ali et al. 2017b, 2018).

101 In the current study, we have reported the synthesis of Ag@NiO by deposition of silver  
102 nanoparticles on the surface of nickel oxide prepared by precipitation method. To ensure its  
103 stability and avoid leaching out in the aqueous medium, Ag@NiO was immobilized in calcium  
104 alginate (Alg) hydrogel beads. To the best of our knowledge, immobilization of Ag@NiO onto  
105 calcium alginate hydrogel beads is not yet reported. Also, no literature has been found on  
106 utilization of Ag@NiO for catalytic reduction of organic pollutants. The catalytic performance of  
107 as-prepared Ag@NiO/Alg hydrogel beads were evaluated for catalytic reduction of organic dyes,  
108 namely, rhodamine B (RhB) and methyl orange (MO).

109

## 110 **Experimental**

## 111 **Materials**

112 Sodium alginate ( $\text{NaC}_6\text{H}_7\text{O}_6$ ) was obtained from Shanghai Aibi Chemistry Preparation Co., Ltd.  
113 Calcium chloride ( $\text{CaCl}_2$ ), Silver nitrate ( $\text{AgNO}_3$ ) and Nickel nitrate hexahydrate ( $\text{NaNO}_3 \cdot 6\text{H}_2\text{O}$ )

114 were purchased from Sigma Aldrich. Sodium borohydride ( $\text{NaBH}_4$ ) was purchased from BDH  
115 Chemical Laboratories, Poole, England. Rhodamine B (RhB) and Methyl orange (MO) were  
116 purchased from Merck. All the chemicals used were of analytical grade and were used without  
117 any further purification process. All solutions were prepared in deionized water obtained from  
118 PCSIR laboratories, Peshawar, Pakistan.

119 **Synthesis of  $\text{Ag@NiO}$  nanocomposite**

120 Firstly, nickel oxide nanoparticles were prepared by precipitation method. Briefly, 10g of  
121  $\text{NiNO}_3 \cdot 6\text{H}_2\text{O}$  was dissolved in 500mL of deionized water, followed by drop-wise addition of  
122 dilute ammonia water solution, until the pH reaches to 8. The precipitates formed were then  
123 filtered, washed with deionized water for several times. The filtered precipitates were then  
124 allowed to dry at 100°C and calcined at 800°C for 24h.

125 For the synthesis of  $\text{Ag@NiO}$  nanocomposite, 0.5g of the preformed NiO nanoparticles was  
126 well-dispersed in water under ultrasonic treatment. Then 0.1M  $\text{AgNO}_3$  was added to the NiO  
127 suspension and sonicated for 1h. The deposited  $\text{Ag}^+$  ions were then reduced with 0.1M  $\text{NaBH}_4$   
128 aqueous solution. The resultant  $\text{Ag@NiO}$  was then filtered, washed, and dried at 80°C.

129 **Synthesis of  $\text{Ag@NiO}/\text{calcium alginate hydrogel beads}$**

130 For the synthesis of  $\text{Ag@NiO}/\text{Alg}$  hydrogel beads,  $\text{Ag@NiO}$  nanomaterial was dispersed well in  
131 20mL of distilled water and added to already prepared alginate solution (with percent  
132 composition of 2% w/v) under vigorous stirring. 0.2M  $\text{CaCl}_2$  solution was prepared by dissolving  
133 14.7g into 500mL. For the preparation of hydrogel beads,  $\text{Ag@NiO}/\text{alginate}$  suspension was  
134 taken in 5cc medical syringe and added drop by drop to  $\text{CaCl}_2$  solution from 10cm height with  
135 continuous stirring at a speed of 50rpm. As soon as the drop fell into the  $\text{Ca}^{2+}$  ions solution, it

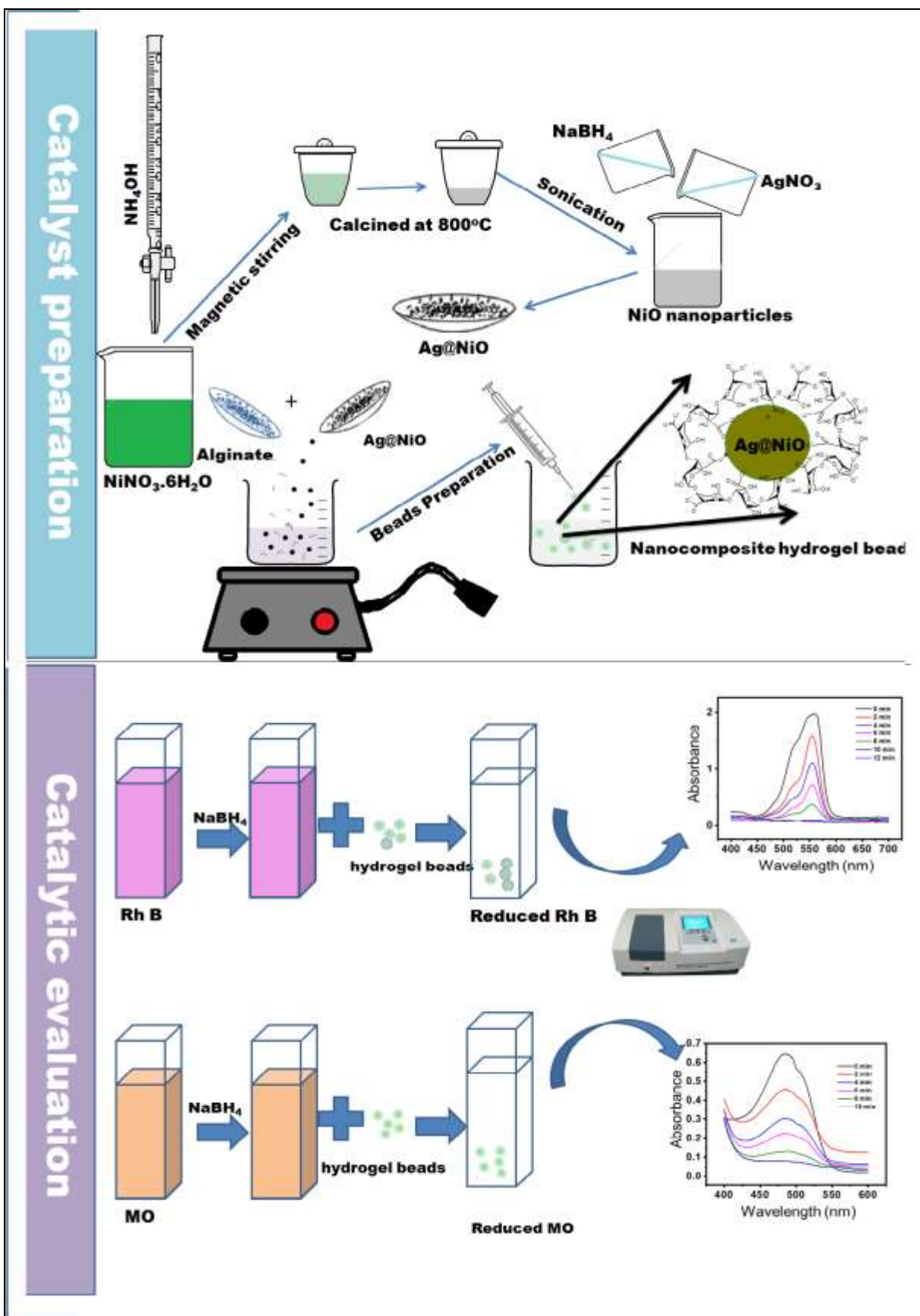
136 attained a solid spherical shape. The same procedure was employed for the formation of pure  
137 calcium alginate beads without the addition of AgNiO nanomaterial.

138 **Characterization**

139 The functional group analysis of Alg, Ag@NiO/Alg and Ag@NiO was conducted by Fourier  
140 transform infrared spectroscopic technique using Perkin Elmer spectrometer at a frequency range  
141 of 450 to 4000cm<sup>-1</sup> with a resolution of 4cm<sup>-1</sup> and 0.2 scanning speed. X-ray Diffraction  
142 technique was used to determine the crystalline nature of Alg, Ag@NiO/Alg and AgNiO with  
143 the help of X-ray diffractometer (model: JDX-3532, JEOL, Japan) using Nickel filtered Cu-K $\alpha$   
144 radiation of 1.5418Å in the 2 $\theta$  range of 5° to 90°. The structural morphology and elemental  
145 maping of the synthesized samples was evaluated by scanning electron microscopic (Model;  
146 JSM5910, JEOL, Japan) and energy-dispersive X-ray diffractometric techniques (using liquid  
147 nitrogen cooled Oxford 7353 EDX detector, Oxford Instruments, Abingdon, United Kingdom),  
148 respectively.

149 **Catalytic Evaluation of Ag@NiO/Alg hydrogel beads**

150 In order to evaluate the catalytic efficiency of Ag@NiO/Alg hydrogel beads, catalytic reduction  
151 of RhB and MO was studied. For this purpose, 2.5mL of RhB (0.05mM) and MO (0.1mM) dye  
152 solution was taken in a quartz cuvette separately, followed by addition of 0.1M NaBH<sub>4</sub> solution.  
153 Then depending on the required reaction conditions, a known amount of the Ag@NiO/Alg  
154 hydrogel beads was added into the reaction system. The decrease in absorbance at the  $\lambda_{max}$  of  
155 the dyes was regularly noted with the help of UV-Vis spectrophotometer after each 2 min.



157 Scheme 1. Preparation of hydrogel beads and its catalytic evaluation for toxic dyes reduction

158

159 **Results and Discussion**

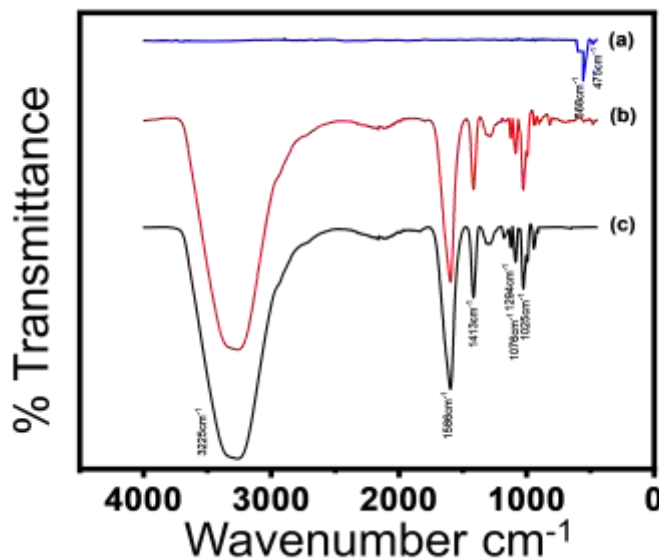
160 Scheme 1 shows the general overview of this research work. The first part consists of preparation  
161 of the Ag@NiO nanomaterial and Ag@NiO/Alg nanocomposite beads (catalyst preparation) and  
162 the second part consists of utilization of the Ag@NiO/Alg nanocomposite beads in the reduction  
163 of RhB and MO dyes (catalytic evaluation). After preparation of the Ag@NiO nanomaterial,  
164 pure Alg, Ag@NiO/Alg nanocomposite beads, they were first subjected to various instrumental  
165 techniques as given in the following text.

166

167 **FTIR Analysis**

168 FTIR spectra of Alg hydrogel, Ag@NiO and Ag@NiO/Alg are shown in Figure 1. The spectral  
169 peaks at  $475\text{cm}^{-1}$  and  $568\text{cm}^{-1}$  corresponds to stretching vibrations of NiO as shown in Figure 1a  
170 (Nagamuthu and Ryu 2019). Ag nanoparticles synthesized by chemical approach do not exhibit  
171 peak in the infra-red region. No appearance of any absorption peak for Ag confirms the synthesis  
172 of metallic silver only in this approach, without the formation of oxides of silver (Beura et al.  
173 2021). The broad absorption band at  $3225\text{cm}^{-1}$  corresponds to the presence of hydroxyl group.  
174 The sharp peaks at  $1586\text{cm}^{-1}$  and  $1413\text{cm}^{-1}$  are attributed to asymmetric and symmetric stretching  
175 vibrations of the carboxylate groups, respectively. Peaks observed at  $1294\text{cm}^{-1}$ ,  $1076\text{cm}^{-1}$ , and  
176  $1025\text{ cm}^{-1}$  are associated with stretching vibrations of C-O functional group of glycosidic  
177 linkage between  $\beta$ -D-mannuronic and R-L-guluronic acid and is an indication of the degree of

178 stability of the linear chain in the alginate (Simonescu et al. 2020). In the FTIR spectrum of  
179 Ag@NiO/Alg all peaks characteristic of Ag@NiO and Ca-Alg can be seen, as represented by  
180 Figure 1b.



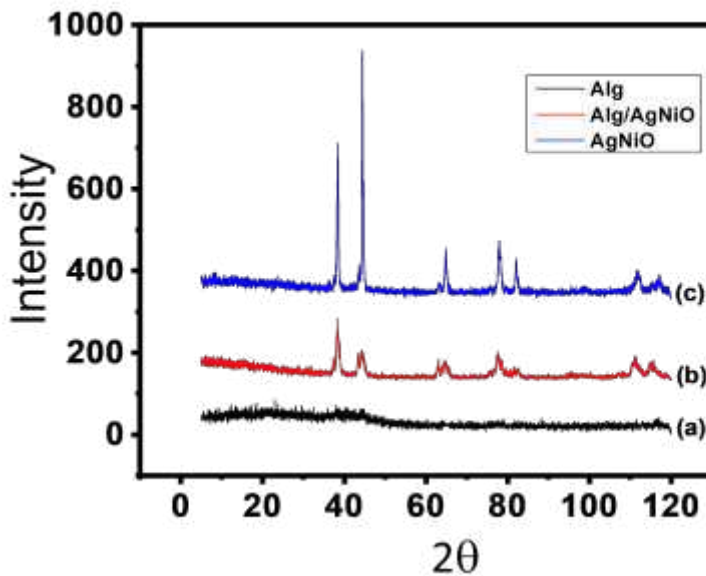
181

182 Figure 1. FTIR spectra for (a) Ag@NiO (b) Ag@NiO/Alg (c) pure Alg.

183 **XRD Analysis**

184 In order to study the crystalline nature of prepared samples, pure Alg, Ag@NiO and  
185 Ag@NiO/Alg were characterized by X-ray diffractrometry technique. Figure 2a represents the  
186 XRD pattern of Alg hydrogel beads. No diffraction peak can be observed which confirms non-  
187 crystalline nature of Alg. Figure 2c indicates the XRD pattern for Ag@NiO nanomaterial. The  
188 diffraction peaks at  $2\theta = 37.22^\circ, 43.25^\circ, 62.83^\circ$  and  $75.34^\circ$  corresponds to the presence of NiO  
189 (JCPDS card No-73-1523) in the sample. Similarly, the peaks at  $2\theta = 38.26^\circ, 44.47^\circ, 64.71^\circ$ ,  
190  $77.74^\circ$  and  $81.91^\circ$  are in good agreement with the presence of metallic silver (JCPDS card No-87-  
191 0719) in the Ag@NiO sample. XRD peaks for nickel oxide and metallic silver coincides with

192 (111), (200), (220), (311) and (222) hkl planes, thus indicating their cubic crystal structures. All  
193 the characteristic peaks were observed in the XRD pattern of ALG/AgNiO hydrogel beads,  
194 which confirms the successful incorporation of AgNiO into the polymer matrix, as can be seen  
195 from Figure 2b.

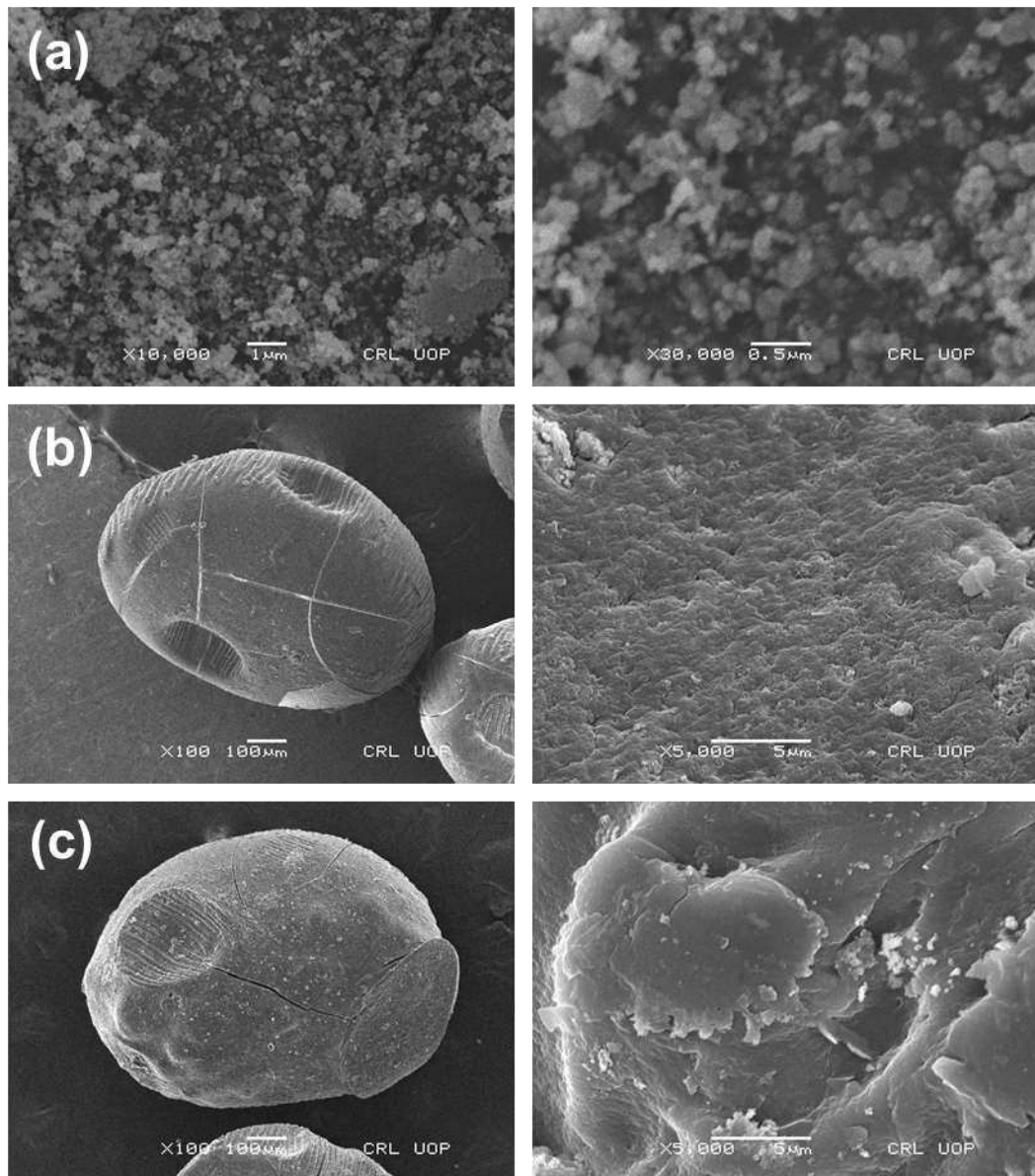


196  
197 Figure 2. XRD pattern of (a) Alg beads (b) Ag@NiO/Alg beads (c) Ag@NiO nanoparticles.  
198

### 199 SEM Analysis

200 The surface features and morphology of pure Alg beads, Ag@NiO nanoparticles and  
201 Ag@NiO/Alg composite beads were characterized by scanning electron microscopy (SEM) as  
202 can be seen in SEM photographs (Figure 3). Figure 3a shows the SEM photographs of Ag@NiO  
203 nanoparticles. No sign of large particles was observed in the low magnification image (Figure 3a,  
204 right side). It can be seen in a left side photograph that all the particle sizes were below 100nm.  
205 Pure Alg hydrogel beads with sizes in the range of 1.5 to 2mm were prepared and subjected to  
206 morphological analysis by SEM. As shown in the left-side SEM photograph in Figure 3b, the

207 pure Alg beads were not completely spherical and indicated the oval shapes with some dents.  
208 The high magnification photograph of the pure Alg beads is given in the right-side of the Figure  
209 3b. It shows porosity in the bead's surface. Figure 3c (left-side) shows the SEM photograph of  
210 Ag@NiO/Alg nanocomposite bead. As compared to the pure Alg beads, the Ag@NiO/Alg  
211 nanocomposite bead surface has small white spots. High magnification SEM photographs in  
212 Figure 3c on left side reveals that the beads surface has small particles. Thus, the SEM analysis  
213 of the Ag@NiO/Alg nanocomposite bead suggest the successful immobilization of Ag@NiO  
214 onto Ca<sup>2+</sup>-Alg hydrogel beads.



215

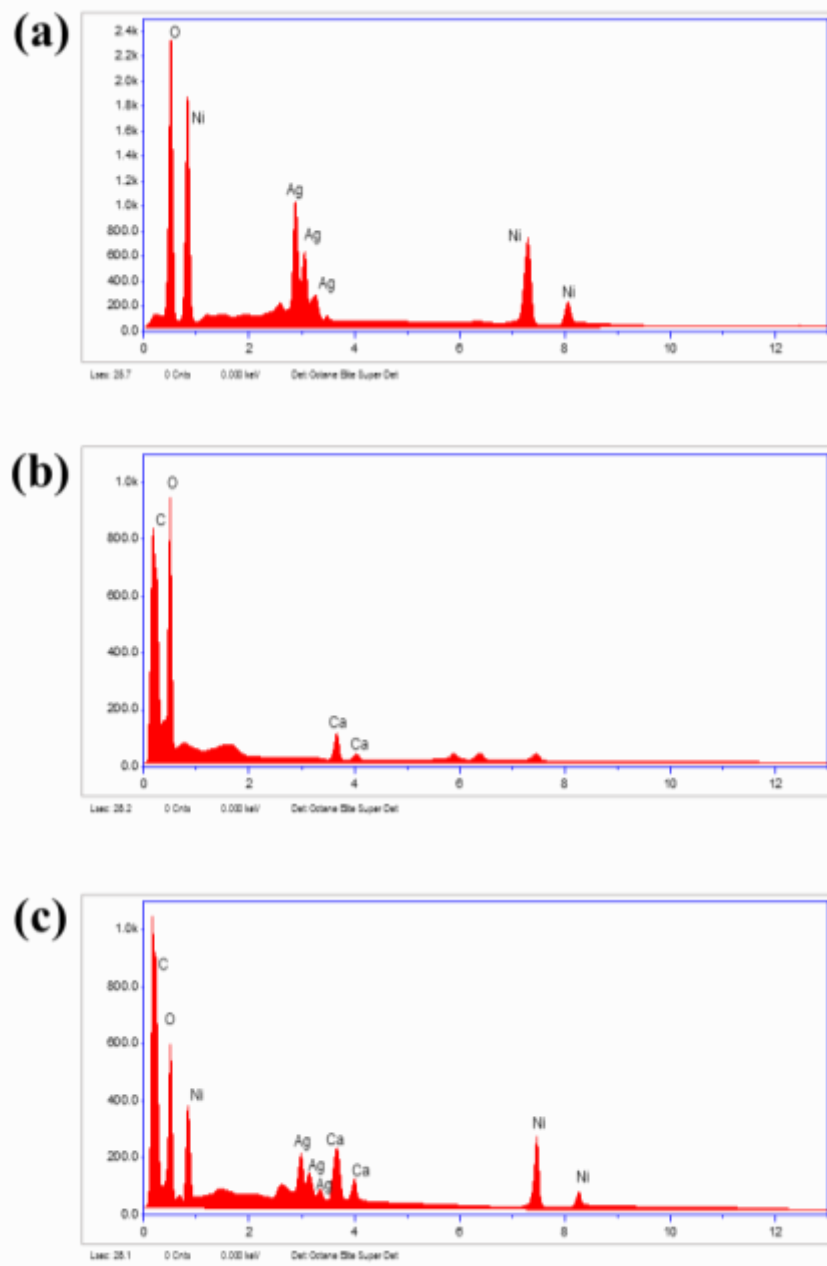
216 Figure 3. SEM photographs of (a) Ag@NiO nanoparticles, (b) Alg beads and (c) Ag@NiO/Alg  
217 beads.

218

219 **EDS Analysis**

220 To explore the elemental constituents of the prepared samples, EDS analyses were carried out for  
221 Ag@NiO nanoparticles, Alg beads and Ag@NiO/Alg beads. The EDS elemental mapping  
222 analyses on the Ag@NiO nanocomposite reveal the presence of Ag, Ni and O elements, as can

223 be seen from Figure 4a. No other elements were detected which confirms that Ag@NiO was  
224 formed in pure form without any external impurities. The EDS spectrum of pure Alg can be seen  
225 from Figure 4b, which constitutes all the characteristic peaks for C, O and Ca, known to be as  
226 principal constituents of calcium alginate hydrogel beads. Fig.4c shows EDS spectrum for  
227 Ag@NiO/Alg hydrogel beads. Prominent peaks at 0.3keV = C, 0.5keV = O and 3.5keV = Ca  
228 indicates the principal constituent elements of calcium crosslinked alginate beads. The presence  
229 of strong peaks at 0.5kev= O, 0.8keV=Ni and 3.0keV=Ag confirms the successful incorporation  
230 of Ag@NiO into calcium alginate hydrogel beads.



231

Figure 4. EDS spectral mapping for (a) Ag@NiO nanoparticles (b) Alg and (c) Ag@NiO/Alg beads.

234 Catalytic Experiments

235

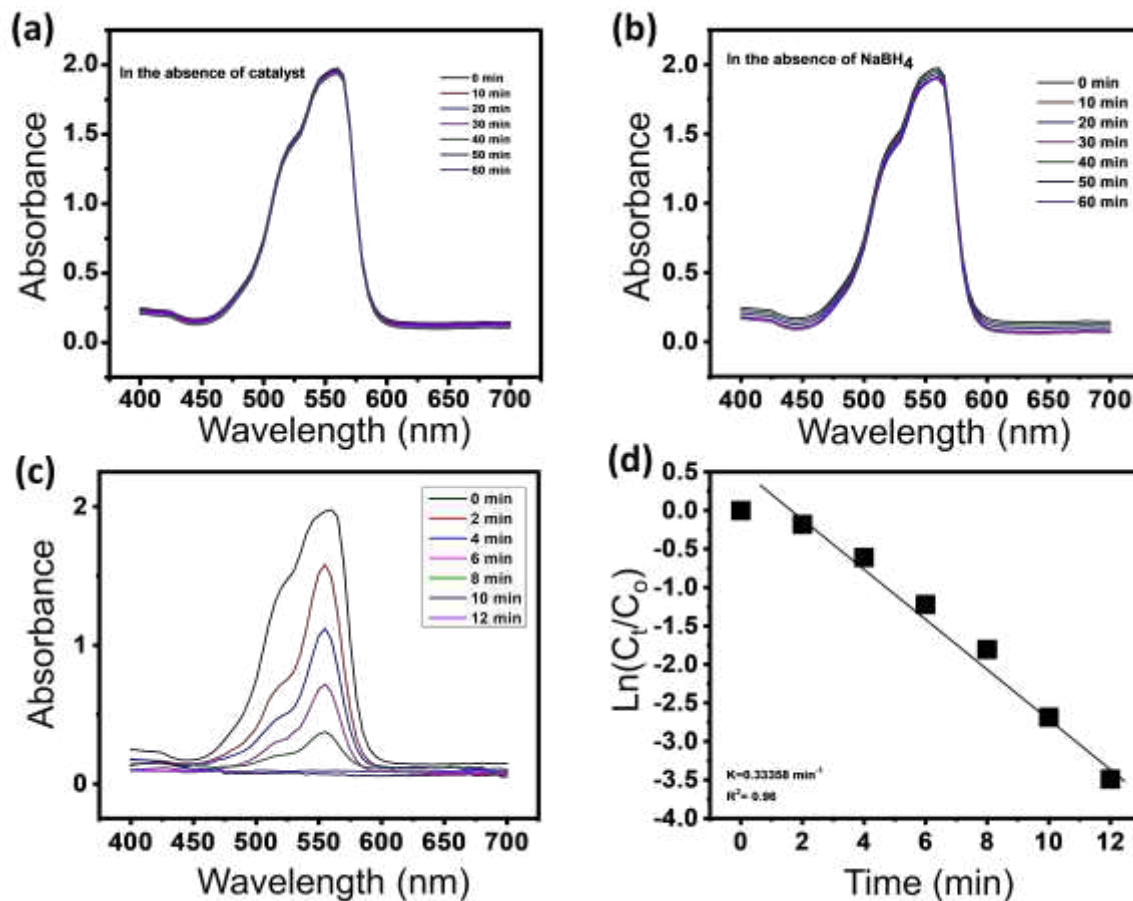
236 Catalytic reduction of RhB

After the successful synthesis of Ag@NiO/Alg and its confirmation by different instrumental techniques, its catalytic efficiency was evaluated by RhB dye reduction. Rhodamine B (Rh-B, [9-(2-carboxyphenyl)-6-diethylamino-3-xanthine]-diethylammonium chloride) is a cationic xanthene dye, widely used in textile and paper industries as well as in fluorescent biotechnology. Despite of its useful aspects, it has adverse effects on the environment, when discharged in untreated form into the water bodies. In order to decline its toxic effects, rendered to it by the presence of  $-N(C_2H_5)$  sites in its structure, its abatement has become crucial. For this purpose, 0.05mM aqueous solution of RhB was processed. Before going for the actual catalytic experiments, absorption spectrum of RhB was observed in the presence of Ag@NiO/Alg only, without the addition of reducing agent. Figure 5b confirms that no adsorption has been taken place with Ag@NiO/Alg. In another batch of experiment, reduction of RhB was studied in the absence of Ag@NiO/Alg using NaBH<sub>4</sub> as a reducing agent. Figure 5a shows UV-Vis absorption spectra for reduction of 2.5mL RhB (0.05mM) dye solution and 1mL of 0.1M NaBH<sub>4</sub>. No notable decrease in the absorption spectrum was observed for upto 1h which indicates that RhB does not undergo self-hydrolysis with mere addition of reducing agent. Catalytic reduction is an electron transfer process between NaBH<sub>4</sub> and dye molecule, where NaBH<sub>4</sub> acts as an electron donor and dye molecule serves as an acceptor. The results from Figure 5a indicate that this electron transfer process is thermodynamically feasible but kinetically un-favourable. For actual practice, 2.5mL of RhB aqueous solution with molar concentration of 0.05mM, 1mL of 0.1M NaBH<sub>4</sub> solution and 0.1g of Ag@NiO/Alg hydrogel beads was placed into a quartz cuvette with a total capacity of 4mL. The decrease in absorption maxima was repeatedly recorded at 554 nm, after an interval of 2 min. Figure 5c shows the time dependent UV-Vis spectra for catalytic reduction of RhB. The disappearance of absorption maxima at 554 nm indicates the complete

conversion of RhB into leuco-rhodamine B (Abay et al. 2017). The rate of reaction  $k_{app}$  was calculated from the linear slope of  $\ln C_t/C_0$  vs. time as can be seen from Figure 5d. Kapp value obtained was found to be equal to  $0.33358 \text{ min}^{-1}$  for this reaction. As  $\text{NaBH}_4$  is used in excess, the reduction reaction is assumed to follow *pseudo-first order* kinetics. The linear coefficient value of  $R^2 = 0.96$  for the correlation between  $\ln C_t/C_0$  and time, validate *pseudo-first order* kinetics for the reduction process.

266

267



268

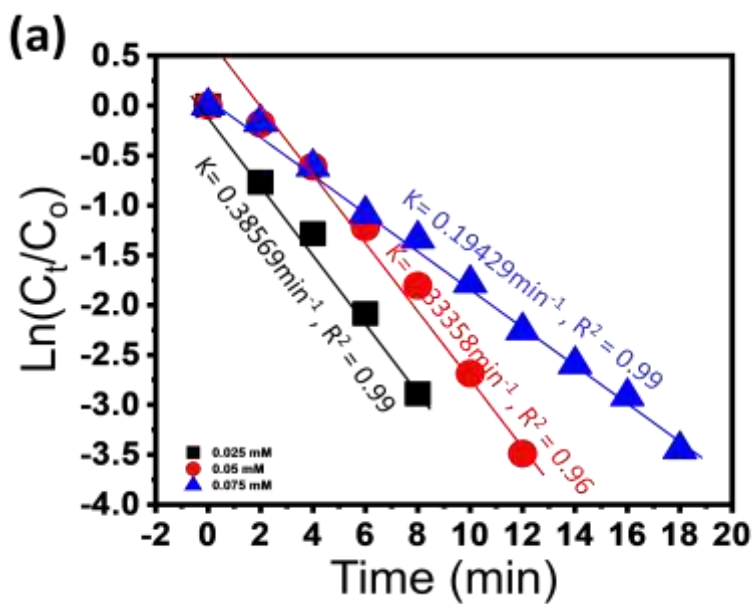
Figure 5. UV-Vis absorption spectra for 0.05mM RhB reduction (a) in the absence of catalyst with 0.1M  $\text{NaBH}_4$  (b) in the absence of  $\text{NaBH}_4$  with 0.1g of catalyst (c) in the presence of 0.1M

271 NaBH<sub>4</sub> and 0.1g of catalyst (d) kinetic plot for reduction of 0.05mM RhB with 0.1M NaBH<sub>4</sub> as a  
272 reducing agent and 0.1g of catalyst

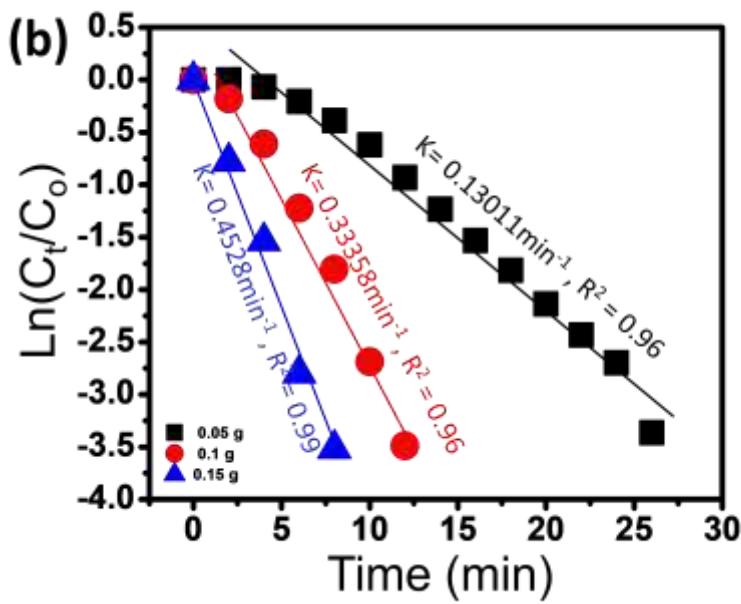
273 For the purpose to investigate the effect of RhB concentration on the reduction kinetics, three  
274 different dye concentrations, say, *0.025mM, 0.05mM and 0.1mM* were studied while keeping all  
275 other condition constant at 0.1M NaBH<sub>4</sub> and 0.1g of hydrogel beads. Figure 6a shows kinetic  
276 plot of  $\ln C_t/C_0$  vs. time at varying dye concentration. The calculated apparent rate constant  
277 values were  $0.38469 \text{ min}^{-1}$ ,  $0.33358 \text{ min}^{-1}$  and  $0.19429 \text{ min}^{-1}$  for dye concentration of 0.025 mM,  
278 0.05 mM and 0.1 mM, respectively.  $R^2$  values were found in the range of 0.96-0.99, which refers  
279 to goodness of the fit. Decrease in reaction rate was observed with increasing dye concentration.  
280 This is because of the fact that catalyst acts as a limiting reagent, when dye concentration, hence  
281 number of dye molecules is increased. Our results are similar to the literature reports as Chook et  
282 al studied the RhB concentration effect on the reaction time and rate constant while using CNF-  
283 AgNPs as a catalyst (Chook et al. 2015). The reaction time was reported to be 5, 12 and 90 min  
284 for the reduction of  $2.0 \times 10^{-4}$ ,  $1.0 \times 10^{-4}$  and  $4.0 \times 10^{-5}$  M dye concentration.

285 In the same manner, reduction of 0.05mM RhB dye was studied at three different catalyst  
286 amounts, that is *0.05g, 0.1g and 0.15g*, concerning to evaluate the effect of catalyst dosage on the  
287 reaction rate. Figure 6b shows kinetic plot of  $\ln C_t/C_0$  with time for reduction of 0.05mM RhB at  
288 varying dye concentration. The *kapp* values at 0.05 g, 0.1 g and 0.15 g were calculated to be  
289  $0.13011 \text{ min}^{-1}$ ,  $0.33358 \text{ min}^{-1}$  and  $0.4528 \text{ min}^{-1}$ , respectively. These values clearly depict that rate  
290 of reaction increased with an increase in catalyst quantity. This increase in *kapp* value is  
291 associated with the increase in number of active sites for the reaction to take place. Similar  
292 results were reported by Maryami et al for the catalytic reduction of Rh B ( $2.09 \times 10^{-5}$  M) in the  
293 presence of 5.0mg, 7.0mg and 10.0mg Pd/Perlite nanocomposite catalyst. A decrease in the

reaction time was observed in the order of 45 min (5.0 mg), 5 min (7.0 mg) and 60 s (10 mg) (Maryami et al. 2017). Further, Zhang et al investigated the effect of Ag dosage on the catalytic reduction of Rh B dye with an initial concentration of 20m/L (Zhang et al. 2021). An increase in the  $k_{app}$  values was reported given as  $0.12 \text{ min}^{-1}$ ,  $0.17 \text{ min}^{-1}$ , and  $0.21 \text{ min}^{-1}$  for  $\text{Fe}_3\text{Pt}-60\text{mL Ag}$ ,  $\text{Fe}_3\text{Pt}-90\text{mL Ag}$  and  $\text{Fe}_3\text{Pt}-120\text{mL Ag}$ , respectively.



299



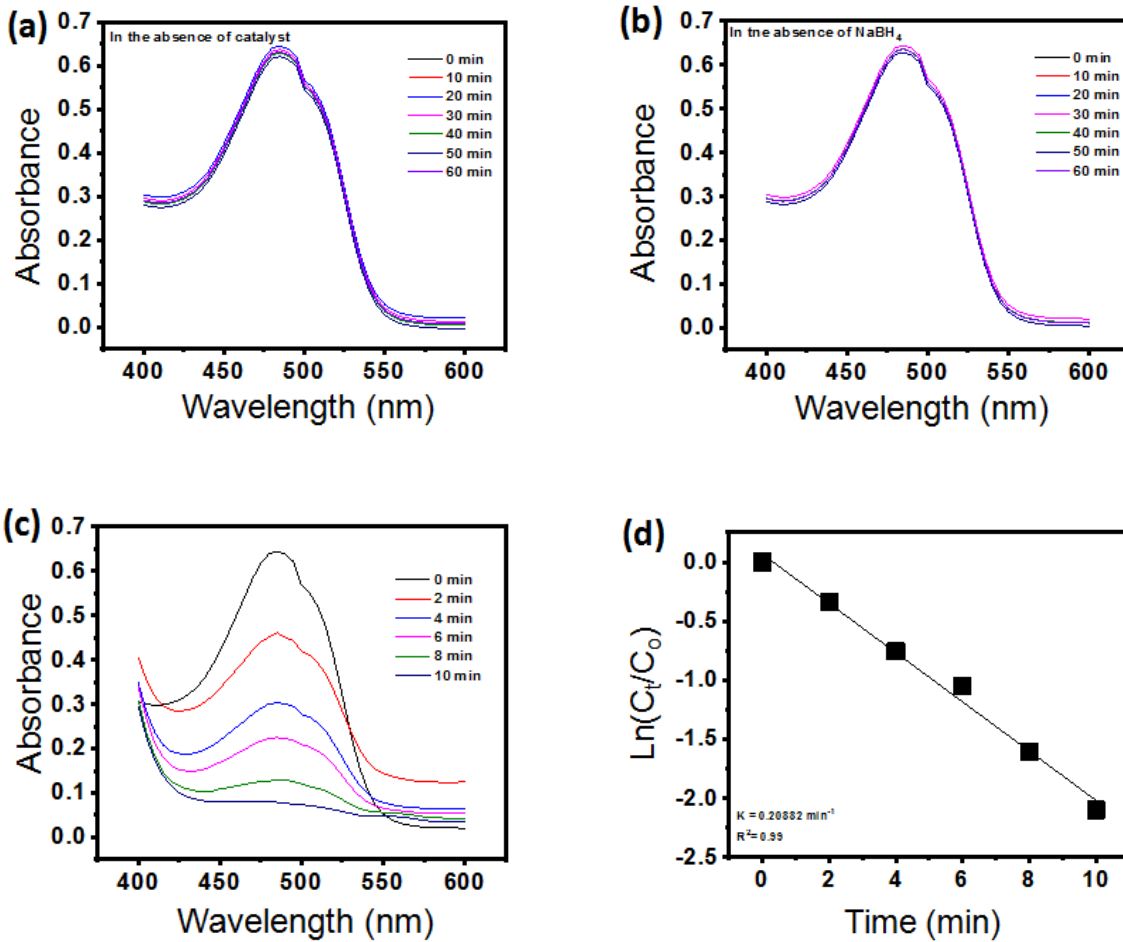
300

301 Figure 6. linear correlation of  $\ln C_t/C_0$  vs. time at (a) varying RhB concentration at 0.1M NaBH<sub>4</sub>  
302 and 0.1g of catalyst and (b) varying catalyst dosage at 0.05mM RhB and 0.1M NaBH<sub>4</sub>

303

304 **Catalytic reduction of MO**

305 Similarly, catalytic efficiency of AgNiO/Alg hydrogel beads was investigated for MO dye  
306 reduction. MO is an anionic azo based dye having  $\lambda_{max}$  at 464 nm in its UV-visible spectrum at  
307 neutral pH. For MO reduction reaction, 2.5mL of MO dye with molar concentration of 0.1mM  
308 and 1mL of 0.1M NaBH<sub>4</sub> was taken into a quartz cuvette, followed by addition of 0.1g of  
309 AgNiO/Alg hydrogel beads. As like in the case of RhB, before going for the actual  
310 experimentation, reduction of MO was investigated for self-hydrolysis with NaBH<sub>4</sub>. No  
311 reduction reaction was observed in the absence of catalyst, as can be seen from Figure 7a. Figure  
312 7b shows absorption spectra for MO dye in the absence of NaBH<sub>4</sub>, which illustrates that no  
313 adsorption of dye occurred on Ag@NiO/Alg surface. Figure 7c shows time dependent UV-Vis  
314 spectra for 0.1mM MO dye in the presence of 0.1M NaBH<sub>4</sub> and 0.1g of Ag@NiO/Alg hydrogel  
315 beads. The progress of reaction was observed from decrease in the absorbance value at 464 nm.  
316 At the end, the observed peak at 464 nm is completely diminished, considered to be due to the  
317 breakage of the -N=N- (azo) bond. Apparent rate constant value was calculated from slope of the  
318 linear plot between  $\ln C_t/C_0$  and time. Figure 7d shows kinetic plot of  $\ln C_t/C_0$  vs. time. Kapp  
319 value was found to be 0.20659 min<sup>-1</sup>. The reaction follows *pseudo-first order* kinetics.



320

321

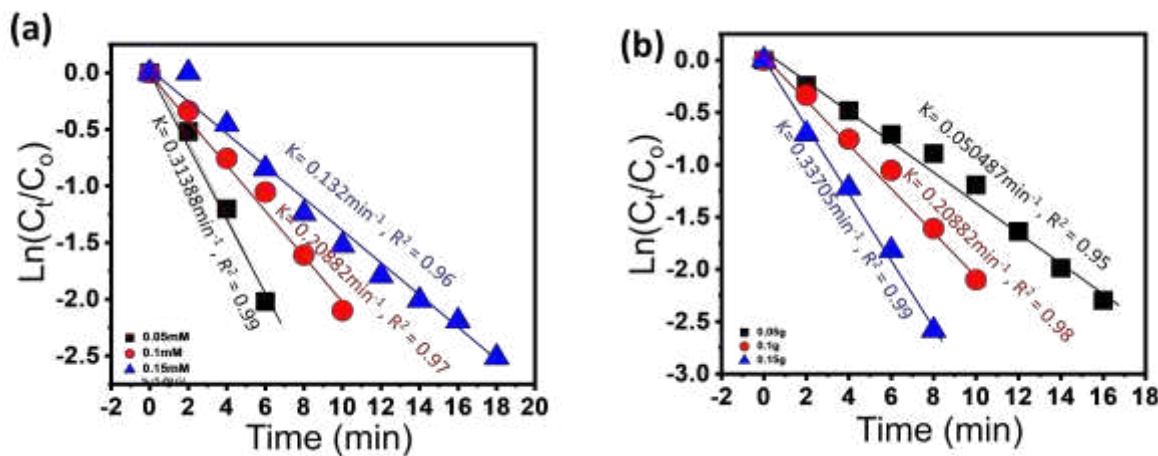
322 Figure 7. UV.Vis absorption spectra for 0.1mM MO reduction (a) in the absence of catalyst with  
 323 0.1M NaBH<sub>4</sub> (b) in the absence of NaBH<sub>4</sub> with 0.1g of catalyst (c) in the presence of 0.1M  
 324 NaBH<sub>4</sub> and 0.1g of catalyst (d) kinetic plot for reduction of 0.1mM MO with 0.1M NaBH<sub>4</sub> as a  
 325 reducing agent and 0.1g of catalyst.

326

327 In order to study the effect of dye concentration on rate of reaction, MO dye reduction was  
 328 studied at three varying concentrations, say, 0.05mM, 0.1mM and 0.15mM, keeping all the other  
 329 parameters constant. Figure 8a shows kinetics plot of lnC<sub>t</sub>/C<sub>0</sub> against time for catalytic reduction  
 330 of MO at varying initial concentrations. Rate constants for these reactions were found to be equal  
 331 to 0.13201 min<sup>-1</sup>, 0.20882 min<sup>-1</sup> and 0.31388 min<sup>-1</sup>, respectively. Hu et al reported a decrease in

332 % decolourization rate with an increase in the initial concentration of MO (10mg/L, 20mg/L,  
 333 30mg/L, 40mg/L and 50mg/L) in the presence of 0.1g of nano-MoS/TiO<sub>2</sub> composite catalyst  
 334 (Hu et al. 2010).

335 Similarly rate of reaction was studied at varying catalyst dosage, keeping concentration of MO  
 336 and NaBH<sub>4</sub> constant. For this purpose, reduction of 0.1mM MO with 0.1M NaBH<sub>4</sub> was studied  
 337 in the presence of three varying catalyst quantities, that is, 0.05g, 0.1g and 0.15g. Figure 8b  
 338 shows plot of lnC<sub>t</sub>/C<sub>0</sub> and time for MO dye reduction at varying catalyst dose. Kapp values were  
 339 estimated to be 0.050487min<sup>-1</sup>, 0.20882 min<sup>-1</sup> and 0.33705 min<sup>-1</sup> at 0.05g, 0.1g and 0.15g  
 340 catalyst dosage, respectively. In a similar manner, Islam et al reported apparent rate constant  
 341 values of  $1.27 \times 10^{-4}$  s<sup>-1</sup>,  $3.36 \times 10^{-3}$  s<sup>-1</sup> and  $4.58 \times 10^{-3}$  s<sup>-1</sup> for MO reduction in the presence of  
 342 pristine CF, CF-AuNPs-0.98 and CF-AuNPs-2.87 (Islam et al. 2017).



343  
 344 Figure 8. Linear correlation of lnC<sub>t</sub>/C<sub>0</sub> vs. time at (a) varying MO concentration at 0.1M NaBH<sub>4</sub>  
 345 and 0.1g of catalyst and (b) varying catalyst dosage at 0.1mM MO and 0.1M NaBH<sub>4</sub>  
 346  
 347 Furthermore, the spectral data of the catalytic reduction of the RhB and MO was also analyzed  
 348 for the possibility to follow other type of reaction kinetics. In addition to the pseudo-first order

349 reaction, the data was analyzed using the following zero (i), pseudo-first (ii),  
350 first (iii) and second (iv) order kinetic equations,

351  $[A] - [A]_0 = -kt$  (i)

352  $\ln[A]/[A]_0 = -kt$  (ii)

353  $\ln[A] = -kt + C$  (iii)

354  $\frac{1}{[A]} - \frac{1}{[A]_0} = kt$  (iv)

355 Where  $[A]$  and  $[A]_0$ , and  $k$  are the dye concentration at a given time, at zero time ( $t$ ) and rate  
356 constant, respectively.

357 Table 1 summarizes  $k_{app}$  and R-square values for the Rh B and MO reduction at varying dye  
358 initial concentration and catalyst dosage. The highest R-square values for any given reaction  
359 suggest that the experimental data was well-fitted to the *pseudo-first order* kinetic equation.

360

361

362 *Table 1. Comparison of Adj.  $R^2$  and  $k_{app}$  values derived from zero order, pseudo 1st order, 1st  
363 order and 2nd order kinetics for Rh B and MO dyes in the presence of  $NaBH_4$  under varying  
364 catalyst dosage and dye concentration.*

Pollutant	Conc.	Catalyst dosage	Zero order $R^2$	Zero order $k_{app}$	Pseudo 1 <sup>st</sup> order $R^2$	Pseudo 1 <sup>st</sup> order $k_{app}$	1 <sup>st</sup> order $R^2$	1 <sup>st</sup> order $k_{app}$	2 <sup>nd</sup> order $R^2$	2 <sup>nd</sup> order $k_{app}$
RhB	0.05mM	0.05g	0.90543	0.07305	0.98494	0.1323	0.98494	0.1323	0.73631	-0.45
	0.05mM	0.1g	0.93152	0.15796	0.98237	0.33358	0.98237	0.33358	0.64391	-1.231
	0.05mM	0.15g	0.98385	0.22035	0.98821	0.45248	0.98821	0.45248	0.39082	-1.768
	0.025mM	0.1g	0.9746	0.2009	0.99347	0.35469	0.99347	0.35469	0.49893	-1.065
	0.075mM	0.1g	0.89553	0.11475	0.99535	0.19429	0.99535	0.19429	0.75601	-0.7111

MO	0.1mM	0.05g	0.92327	0.03306	0.97437	0.13229	0.97437	0.13229	0.88824	-0.719
	0.1mM	0.1g	0.94178	0.05577	0.98836	0.20882	0.98836	0.20882	0.83499	-1.049
	0.1mM	0.15g	0.83672	0.0765	0.99442	0.31388	0.99442	0.31388	0.79715	-2.038
	0.05mM	0.1g	0.96787	0.0615	0.9346	0.32506	0.9346	0.32506	0.70416	-2.35
	0.15mM	0.1g	0.77062	0.05328	0.97804	0.15111	0.97804	0.15111	0.94241	-0.629

365

366 A number of researchers' groups put forward different approaches for the successful abatement  
 367 of RhB and MO. Table 2 summarizes the reaction conditions and  $k_{app}$  values for the reduction of  
 368 the above mentioned toxic dyes in the presence of different catalytic systems, reported earlier in  
 369 the literature. Ref (Zhang et al. 2021) reported a novel multifunctional Fe3Pt–Ag nanoparticles  
 370 for the SERS detection and its catalytic reduction. The highest rate constant of  $021\text{min}^{-1}$  was  
 371 observed which was lower than our study. Similarly, Wang et al prepared porous carbon  
 372 protected magnetite and AgNPs (Wang et al. 2013). Besides cell imaging, the  $\text{Fe}_3\text{O}_4@\text{C}-\text{Ag}$   
 373 hybrid NPs showed a good reduction rate constant  $014\text{min}^{-1}$  for the RhB. Mishra et al  
 374 synthesized a  $\text{Fe}_3\text{O}_4-\text{MnO}_2$  nanocomposites by a green method for the  $\text{sp}^3$  C–H  
 375 functionalization of 2-methylpyridine and RhB reduction (Mishra et al. 2016). Their catalyst  
 376 reduced the RhB with a rate constant of  $0.08\text{s}^{-1}$ . Arpit et al also used a green method of using  
 377 *Cladosporium oxysporum* AJP03 for the synthesis of gold nanoparticles (Bhargava et al. 2016).  
 378 The AuNPs were catalytically evaluated in the the reduction of RhB and its effectiveness was  
 379 reported to be  $1.3 \times 10^{-3} \text{ s}^{-1}$ . Similarly, many research studies used the MO as a model reducible  
 380 dye to test the catalysts. In ref (Ahsan et al. 2019), the authors prepared magnetic cobalt  
 381 nanoparticles on a porous carbon support using metal organic frameworks as templates. The  
 382 prepared magnetic C@Co nanocatalyst catalyzed the reduction of MO with a  $0.041\text{s}^{-1}$ . In ref  
 383 (Gupta et al. 2011), three different type of noble metal (Ag, Au and Pt) nanoparticles using a

384 green tannic acid reducing agent. The MO dye reduction rate constant of  $0.0029\text{min}^{-1}$  was  
 385 experimentally measured for the PtNPs. Similarly, 5,7-dihydroxy-6-methoxy-  
 386 3',4'methylenedioxyisoflavone (Dalspinin) stabilized AuNPs (Umamaheswari et al. 2018) and  
 387 poly(methacrylic acid) (p(MAc)) microgels stabilized nickel nanoparticles (Ajmal et al. 2014)  
 388 were used for the MO reduction. The reduction rate constants of  $1.7 \times 10^{-3}\text{s}^{-1}$  and  $0.002\text{s}^{-1}$  were  
 389 reported for the DLP-AuNPs and p(MAc)-Ni catalysts. Ag@NiO/Alg hydrogel beads in this  
 390 research show best catalytic activity of all the catalytic systems enlisted in Table 1, evident from  
 391 their rate constant values.

392

393 *Table 2. Comparison of catalytic activity of Ag@NiO/Alg with previously reported work.*

Pollutant	Catalyst	Dye conc.	Dye vol.	NaBH <sub>4</sub> conc.	NaBH <sub>4</sub> vol.	Rate constant	Ref.
MO	RhB	Fe <sub>3</sub> Pt-120 mL Ag	20 mg L <sup>-1</sup>	2mL	0.1M	0.5mL	$0.21\text{ min}^{-1}$ (Zhang et al. 2021)
		Fe <sub>3</sub> O <sub>4</sub> @C-Ag hybrid NPs	$2 \times 10^{-5}$ mol/L	5mL	0.01 mol/L	10mL	$0.14\text{min}^{-1}$ (Wang et al. 2013)
		Fe <sub>3</sub> O <sub>4</sub> -MnO <sub>2</sub> NCs	0.025mM	2 mL	0.2M	0.4mL	$0.08\text{s}^{-1}$ (Mishra et al. 2016)
		AuNPs	$2.5 \times 10^{-5}$ M		$5 \times 10^{-3}$ M		$1.3 \times 10^{-3}\text{s}^{-1}$ (Bhargava et al. 2016)
		AgNiO/Alg C@Co	0.05mM 20ppm	2.5mL 4mL	0.1M 0.1M	1mL 0.5mL	$0.33358\text{ min}^{-1}$ Present work $0.041\text{s}^{-1}$ (Ahsan et al. 2019)
		Pt NPs	$5 \times 10^{-3}$ M	50µL	0.5%	100µL	$0.0029\text{min}^{-1}$ (Gupta et al. 2011)
		DLP-AuNPs	$1 \times 10^{-4}$ M	3 mL	$1 \times 10^{-3}$ M	-	$1.7 \times 10^{-3}\text{s}^{-1}$ (Umamaheswari et al. 2018)
		p(MAc)-Ni	$4 \times 10^{-4}$ M	50mL	0.756g	-	$0.002\text{s}^{-1}$ (Ajmal et al. 2014)
		AgNiO/Alg	0.05mM	2.5mL	0.1M	1mL	$0.20882\text{min}^{-1}$ Present work

394

### 395 Statistical analysis

396 In order to validate the experimental conditions, simple linear regression model, variance of  
 397 coefficients and ANOVA has been applied to catalytic reduction of Rh B and MO dyes. the data  
 398 obtained from simple linear regression has been summarized in Table 4. Adjacent R<sup>2</sup> value

399 above 0.9 for all of the given data showed that the experimental data is highly significant and  
 400 also indicated goodness of the fit. Furthermore, significance of the experimental data was  
 401 validated by the ANOVA calculations, as can be concluded from p-values (=0.000) in Table 3.  
 402 Table 5 shows variance of co efficient for the reduction of Rh B and MO under varying  
 403 conditions of Alg@AgNiO and dye concentration. It can be concluded that the given table is  
 404 highly significant (with lower p-values than the chosen alpha values).

405

406 Table 3.

407 *Table 3. ANOVA table for RhB and MO reduction in the presence of 0.1g Of Alg@AgNiO and*  
 408 *0.1M NaBH<sub>4</sub>.*

Model		DF	Sum of Squares	Mean Square	F Value	Sig.
RhB	Regression	1	9.9294	9.9294	141.38345	0.000
	Residual	5	0.35115	0.07023		
	Total	6	10.28055			
MO	Regression	1	3.05241	3.05241	425.44726	0.000
	Residual	4	0.0287	0.00717		
	Total	5	3.0811			

409  
 410

*Table 4. Regression Model for Rh B and MO dye reduction under varying conditions of dye concentration and catalyst dosage.*

Pollutant	Conc.	Catalyst dosage	R	R square	Adjusted R square	Error
RhB	0.05mM	0.05g	0.99226	0.98458	0.98303	0.10424
	0.05mM	0.1g	0.99292	0.98589	0.98237	0.16693
	0.05mM	0.15g	0.99557	0.99116	0.98821	0.15605
	0.025mM	0.1g	0.99755	0.9951	0.99347	0.09087
	0.075mM	0.1g	0.99864	0.99728	0.99689	0.06106
MO	0.1mM	0.05g	0.99229	0.98465	0.98245	0.10492
	0.1mM	0.1g	0.99533	0.99069	0.98836	0.0847
	0.1mM	0.15g	0.99791	0.99582	0.99442	0.07428
	0.05mM	0.1g	0.99513	0.99028	0.98542	0.10561
	0.15mM	0.1g	0.99035	0.98079	0.97804	0.12383

411  
 412  
 413

*Table 5. Variance of coefficients for Rh B and MO dye reduction with varying catalyst and dye concentration in the presence of NaBH<sub>4</sub>.*

Unstandardized Coefficients	Standardized Coefficients
-----------------------------	---------------------------

<b>Model</b>	<b>Pollutant</b>	<b>B</b>	<b>Std. Error</b>	<b>Beta</b>	<b>T</b>	<b>Sig.</b>
(Constant)		0.738	0.095		7.735	0.000
0.05g Alg@AgNiO	Rh B 0.05mM	-0.146	0.006	-0.992	-25.266	0.000
(Constant)		0.358	0.181		1.984	0.104
0.1g Alg@AgNiO	Rh B 0.05mM	-0.298	0.025	-0.983	-11.891	0.000
(Constant)		0.084	0.121		0.695	0.537
0.15g Alg@AgNiO	Rh B 0.05mM	-0.452	0.025	-0.996	-18.339	0.000
(Constant)		0.014	0.070		0.194	0.859
0.1g Alg@AgNiO	Rh B 0.025mM	-0.355	0.014	-0.998	-24.688	0.000
(Constant)		0.129	0.047		2.739	0.025
0.1g Alg@AgNiO	Rh B 0.075mM	-0.194	0.004	-0.998	-43.919	0.000
(Constant)		0.099	0.064		1.533	0.169
0.05g Alg@AgNiO	MO 0.1mM	-0.143	0.007	-0.992	-21.187	0.000
(Constant)		0.068	0.061		1.117	0.327
0.1g Alg@AgNiO	MO 0.1mM	-0.209	0.010	-0.995	-20.627	0.000
(Constant)		-0.011	0.058		-0.183	0.867
0.15g Alg@AgNiO	MO 0.1mM	-0.314	0.012	-0.998	-26.726	0.000
(Constant)		0.076	0.088		0.860	0.480
0.1g Alg@AgNiO	MO 0.05mM	-0.337	0.024	-0.995	-14.272	0.005
(Constant)		0.068	0.061		1.117	0.327
0.1g Alg@AgNiO	MO 0.1mM	-0.209	0.010	-0.995	-20.627	0.000
(Constant)		0.074	0.071		1.053	0.323
0.1g Alg@AgNiO	MO 0.15mM	-0.148	0.007	-0.992	-22.346	0.000

414

415 **Reusability tests**

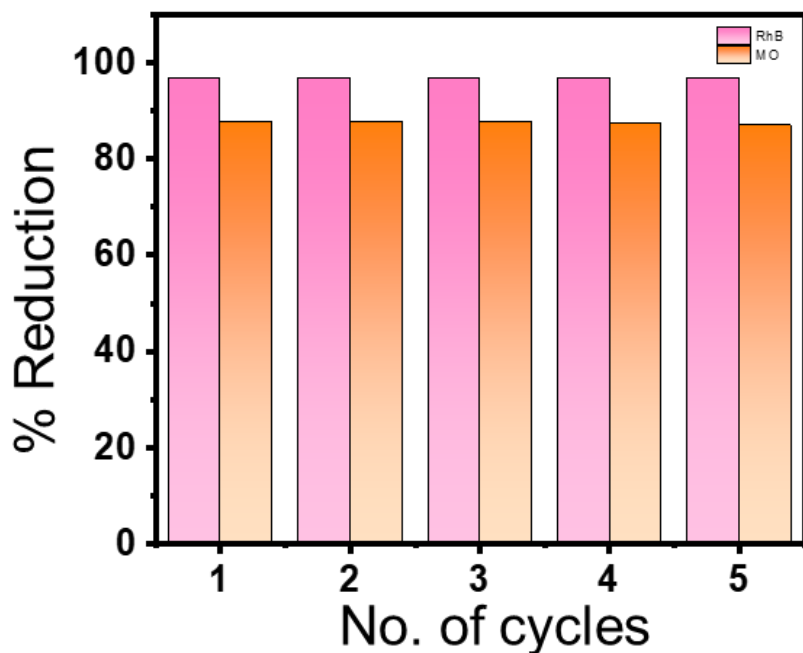
416 Recyclability is a key factor for evaluating catalytic efficiency in heterogeneous catalysis.  
 417 Although Ag@NiO/Alg exhibited high catalytic activity, it is crucial to study the stability of the  
 418 nanocatalyst. Therefore, 0.1g of Ag@NiO/Alg was utilized for reduction of 0.05 mM RhB and  
 419 0.1mM MO (2.5 mL each in a separate batch of reactions) with 1 mL of 0.1M NaBH<sub>4</sub> solution.  
 420 After the completion of reaction, Ag@NiO/Alg hydrogel beads were recovered from the reaction  
 421 media, washed with deionized water and reutilized in another series of reaction. The same  
 422 process was repeated for upto five cycles. % reduction for each successive cycle was calculated  
 423 by using the formula;

424      Percentage % of decolorization =  $\frac{\text{Initial dye concentration} - \text{Final dye concentration}}{\text{Initial dye concentration}} \times 100$

425

426      Figure 9 shows that % reduction of the catalyst remained unaffected (96-97% for RhB and 87-  
427      88% for MO) for up to five consecutive cycles which confirms the high stability of Ag@NiO  
428      inside Ca<sup>2+</sup>-Alg hydrogel beads.

429



430

431      Figure 9. Reusability test results of Ag@NiO/Alg beads.

### 432      Conclusion

433      In summary, Ag nanoparticles were immobilized on NiO, followed by incorporation into calcium  
434      alginate hydrogel beads, by ionotropic crosslinking procedure. The as prepared Ag@NiO/Alg

435 hydrogel beads were characterized by XRD, SEM, FTIR and EDS techniques. The catalytic  
436 activity of Ag@NiO/Alg was evaluated against catalytic reduction of two toxic organic  
437 pollutants, RhB and MO, in the presence of sodium borohydride as a reducing agent. The  
438 calculated kapp values revealed it as an excellent catalyst. Furthermore, ease of its separation  
439 from reaction medium and its recyclability upto five cycles, without any noticeable change in its  
440 catalytic activity, provided evidence for Ag@NiO/Alg as an efficient catalytic system.

441

442 **Declaration of competing interest**

443 The authors report no conflicting interest in any capacity, competing, or financial.

444      **References**

- 445      Abay AK, Chen X, Kuo D-H (2017) Highly efficient noble metal free copper nickel oxysulfide  
446      nanoparticles for catalytic reduction of 4-nitrophenol, methyl blue, and rhodamine-B  
447      organic pollutants. *New J Chem* 41:5628–5638. <https://doi.org/10.1039/C7NJ00676D>
- 448      Ahsan MdA, Fernandez-Delgado O, Deemer E, et al (2019) Carbonization of Co-BDC MOF  
449      results in magnetic C@Co nanoparticles that catalyze the reduction of methyl orange and  
450      4-nitrophenol in water. *J Mol Liq* 290:111059.  
451      <https://doi.org/10.1016/j.molliq.2019.111059>
- 452      Ajmal M, Siddiq M, Al-Lohedan H, Sahiner N (2014) Highly versatile p(MAc)–M (M: Cu, Co,  
453      Ni) microgel composite catalyst for individual and simultaneous catalytic reduction of  
454      nitro compounds and dyes. *RSC Adv* 4:59562–59570.  
455      <https://doi.org/10.1039/C4RA11667D>
- 456      Al-Ghamdi YO, Khan SA (2020) Stabilization of zero-valent Au nanoparticles on  
457      carboxymethyl cellulose layer coated on chitosan-CBV 780 zeolite Y sheets: assessment  
458      in the reduction of 4-nitrophenol and dyes. *Cellulose* 27:8827–8841.  
459      <https://doi.org/10.1007/s10570-020-03379-0>
- 460      Ali F, Khan SB, Kamal T, et al (2017a) Anti-bacterial chitosan/zinc phthalocyanine fibers  
461      supported metallic and bimetallic nanoparticles for the removal of organic pollutants.  
462      *Carbohydr Polym* 173:676–689. <https://doi.org/10.1016/j.carbpol.2017.05.074>
- 463      Ali F, Khan SB, Kamal T, et al (2017b) Chitosan coated cotton cloth supported zero-valent  
464      nanoparticles: Simple but economically viable, efficient and easily retrievable catalysts.  
465      *Sci Rep* 7:16957. <https://doi.org/10.1038/s41598-017-16815-2>
- 466      Ali F, Khan SB, Kamal T, et al (2017c) Bactericidal and catalytic performance of green  
467      nanocomposite based-on chitosan/carbon black fiber supported monometallic and  
468      bimetallic nanoparticles. *Chemosphere* 188:588–598.  
469      <https://doi.org/10.1016/j.chemosphere.2017.08.118>
- 470      Ali N, Awais, Kamal T, et al (2018) Chitosan-coated cotton cloth supported copper nanoparticles  
471      for toxic dye reduction. *Int J Biol Macromol* 111:832–838.  
472      <https://doi.org/10.1016/j.ijbiomac.2018.01.092>
- 473      Asadi S, Eris S, Azizian S (2018) Alginate-Based Hydrogel Beads as a Biocompatible and  
474      Efficient Adsorbent for Dye Removal from Aqueous Solutions. *ACS Omega* 3:15140–  
475      15148. <https://doi.org/10.1021/acsomega.8b02498>
- 476      Atta-ul-Haq, Saeed M, Jamal MA, et al (2019) Green Synthesis of Ag–NiO and Investigation of  
477      its Catalytic Activity for Degradation of Rhodamine B Dye in Aqueous Medium. *Z Für  
478      Phys Chem* 233:1047–1059. <https://doi.org/10.1515/zpch-2018-1226>

- 479 Bagtache R, Sebai I, Abdmeziem K, Trari M (2019) Visible light induced H<sub>2</sub> evolution on the  
480 hetero-junction Ag/NiO prepared by nitrate route. *Sol Energy* 177:652–656.  
481 <https://doi.org/10.1016/j.solener.2018.11.066>
- 482 Beura R, Pachaiappan R, Paramasivam T (2021) Photocatalytic degradation studies of organic  
483 dyes over novel Ag-loaded ZnO-graphene hybrid nanocomposites. *J Phys Chem Solids*  
484 148:109689. <https://doi.org/10.1016/j.jpcs.2020.109689>
- 485 Bhargava A, Jain N, Khan MA, et al (2016) Utilizing metal tolerance potential of soil fungus for  
486 efficient synthesis of gold nanoparticles with superior catalytic activity for degradation of  
487 rhodamine B. *J Environ Manage* 183:22–32.  
488 <https://doi.org/10.1016/j.jenvman.2016.08.021>
- 489 Chanthiwong M, Mongkolthanaruk W, Eichhorn SJ, Pinitsoontorn S (2020) Controlling the  
490 processing of co-precipitated magnetic bacterial cellulose/iron oxide nanocomposites.  
491 *Mater Des* 196:109148. <https://doi.org/10.1016/j.matdes.2020.109148>
- 492 Chen Y, Chen S, Wang B, et al (2017a) TEMPO-oxidized bacterial cellulose nanofibers-  
493 supported gold nanoparticles with superior catalytic properties. *Carbohydr Polym*  
494 160:34–42. <https://doi.org/10.1016/j.carbpol.2016.12.020>
- 495 Chen Z, Zhao B, Fu X-Z, et al (2017b) CuO nanorods supported Pd nanoparticles as high  
496 performance electrocatalysts for glucose detection. *J Electroanal Chem* 807:220–227.  
497 <https://doi.org/10.1016/j.jelechem.2017.11.041>
- 498 Chook SW, Chia CH, Chan CH, et al (2015) A porous aerogel nanocomposite of silver  
499 nanoparticles-functionalized cellulose nanofibrils for SERS detection and catalytic  
500 degradation of rhodamine B. *RSC Adv* 5:88915–88920.  
501 <https://doi.org/10.1039/C5RA18806G>
- 502 Gan L, Li H, Chen L, et al (2018) Graphene oxide incorporated alginate hydrogel beads for the  
503 removal of various organic dyes and bisphenol A in water. *Colloid Polym Sci* 296:607–  
504 615. <https://doi.org/10.1007/s00396-018-4281-3>
- 505 Gupta N, Singh HP, Sharma RK (2011) Metal nanoparticles with high catalytic activity in  
506 degradation of methyl orange: An electron relay effect. *J Mol Catal Chem* 335:248–252.  
507 <https://doi.org/10.1016/j.molcata.2010.12.001>
- 508 Hu KH, Hu XG, Xu YF, Sun JD (2010) Synthesis of nano-MoS<sub>2</sub>/TiO<sub>2</sub> composite and its  
509 catalytic degradation effect on methyl orange. *J Mater Sci* 45:2640–2648.  
510 <https://doi.org/10.1007/s10853-010-4242-9>
- 511 Islam MdT, Dominguez N, Ahsan MdA, et al (2017) Sodium rhodizonate induced formation of  
512 gold nanoparticles supported on cellulose fibers for catalytic reduction of 4-nitrophenol  
513 and organic dyes. *J Environ Chem Eng* 5:4185–4193.  
514 <https://doi.org/10.1016/j.jece.2017.08.017>

- 515 Jamee R, Siddique R (2019) Biodegradation of synthetic dyes of textile effluent by  
516 microorganisms: an environmentally and economically sustainable approach. *Eur J*  
517 *Microbiol Immunol* 9:114–118. <https://doi.org/10.1556/1886.2019.00018>
- 518 Jiang H, Yu C, Huang Z, Zhu H (2019) Oxide(SnO<sub>2</sub>,CeO<sub>2</sub>,Co<sub>3</sub>O<sub>4</sub> and NiO)-Promoted Pt/C  
519 Electrocatalysts for PEMFCs. *ECS Trans* 17:347–358. <https://doi.org/10.1149/1.3142764>
- 520 Kamal T, Ahmad I, Khan SB, Asiri AM (2019) Anionic polysaccharide stabilized nickel  
521 nanoparticles-coated bacterial cellulose as a highly efficient dip-catalyst for pollutants  
522 reduction. *React Funct Polym* 145:104395.  
523 <https://doi.org/10.1016/j.reactfunctpolym.2019.104395>
- 524 Kamal T, Khan SB, Asiri AM (2016) Synthesis of zero-valent Cu nanoparticles in the chitosan  
525 coating layer on cellulose microfibers: evaluation of azo dyes catalytic reduction.  
526 *Cellulose* 23:1911–1923. <https://doi.org/10.1007/s10570-016-0919-9>
- 527 Kamal T, Ul-Islam M, Khan SB, Asiri AM (2015) Adsorption and photocatalyst assisted dye  
528 removal and bactericidal performance of ZnO/chitosan coating layer. *Int J Biol*  
529 *Macromol* 81:584–590. <https://doi.org/10.1016/j.ijbiomac.2015.08.060>
- 530 Kao K-C, Kuroiwa Y, Nishi H, Tatsuma T (2017) Hydrogen evolution from water based on  
531 plasmon-induced charge separation at a TiO<sub>2</sub>/Au/NiO/Pt system. *Phys Chem Chem*  
532 *Phys* 19:31429–31435. <https://doi.org/10.1039/C7CP06527B>
- 533 Karimi-Maleh H, Kumar BG, Rajendran S, et al (2020) Tuning of metal oxides photocatalytic  
534 performance using Ag nanoparticles integration. *J Mol Liq* 314:113588.  
535 <https://doi.org/10.1016/j.molliq.2020.113588>
- 536 Karunamoorthy S, Velluchamy M (2018) Design and synthesis of bandgap tailored porous  
537 Ag/NiO nanocomposite: an effective visible light active photocatalyst for degradation of  
538 organic pollutants. *J Mater Sci Mater Electron* 29:20367–20382.  
539 <https://doi.org/10.1007/s10854-018-0172-0>
- 540 Katheresan V, Kansedo J, Lau SY (2018) Efficiency of various recent wastewater dye removal  
541 methods: A review. *J Environ Chem Eng* 6:4676–4697.  
542 <https://doi.org/10.1016/j.jece.2018.06.060>
- 543 Khalil A, Ali N, Khan A, et al (2020) Catalytic potential of cobalt oxide and agar nanocomposite  
544 hydrogel for the chemical reduction of organic pollutants. *Int J Biol Macromol*  
545 164:2922–2930. <https://doi.org/10.1016/j.ijbiomac.2020.08.140>
- 546 Khan MSJ, Khan SB, Kamal T, Asiri AM (2020) Catalytic Application of Silver Nanoparticles  
547 in Chitosan Hydrogel Prepared by a Facile Method. *J Polym Environ* 28:962–972.  
548 <https://doi.org/10.1007/s10924-020-01657-3>
- 549 Khan SA, Khan SB, Kamal T, et al (2016a) Recent Development of Chitosan Nanocomposites  
550 for Environmental Applications. *Recent Pat Nanotechnol* 10:181–188.  
551 <https://doi.org/10.2174/1872210510666160429145339>

- 552 Khan SB, Khan SA, Marwani HM, et al (2016b) Anti-bacterial PES-cellulose composite spheres:  
553 dual character toward extraction and catalytic reduction of nitrophenol. RSC Adv  
554 6:110077–110090. <https://doi.org/10.1039/c6ra21626a>
- 555 Lam W-H, Chong MN, Horri BA, et al (2017) Physicochemical stability of calcium alginate  
556 beads immobilizing TiO<sub>2</sub> nanoparticles for removal of cationic dye under UV irradiation.  
557 J Appl Polym Sci 134:.. <https://doi.org/10.1002/app.45002>
- 558 Maryami M, Nasrollahzadeh M, mehdipour E, Sajadi SM (2017) Green synthesis of the  
559 Pd/perlite nanocomposite using Euphorbia neriifolia L. leaf extract and evaluation of its  
560 catalytic activity. Sep Purif Technol 184:298–307.  
561 <https://doi.org/10.1016/j.seppur.2017.05.003>
- 562 Mishra K, Poudel TN, Basavegowda N, Lee YR (2016) Enhanced catalytic performance of  
563 magnetic Fe<sub>3</sub>O<sub>4</sub>–MnO<sub>2</sub> nanocomposites for the decolorization of rhodamine B,  
564 reduction of 4-nitroaniline, and sp<sub>3</sub> C–H functionalization of 2-methylpyridines to  
565 isatins. J Catal 344:273–285. <https://doi.org/10.1016/j.jcat.2016.09.020>
- 566 Nagamuthu S, Ryu K-S (2019) Synthesis of Ag/NiO Honeycomb Structured Nanoarrays as the  
567 Electrode Material for High Performance Asymmetric Supercapacitor Devices. Sci Rep  
568 9:1–11. <https://doi.org/10.1038/s41598-019-41446-0>
- 569 Ngo Y-LT, Hoa LT, Chung JS, Hur SH (2017) Multi-dimensional Ag/NiO/reduced graphene  
570 oxide nanostructures for a highly sensitive non-enzymatic glucose sensor. J Alloys  
571 Compd 712:742–751. <https://doi.org/10.1016/j.jallcom.2017.04.131>
- 572 Sahoo PK, Thakur D, Bahadur D, Panigrahy B (2016) Highly efficient and simultaneous  
573 catalytic reduction of multiple dyes using recyclable RGO/Co dendritic nanocomposites  
574 as catalyst for wastewater treatment. RSC Adv 6:106723–106731.  
575 <https://doi.org/10.1039/C6RA23621A>
- 576 Silva KMMN, de Carvalho DÉL, Valente VMM, et al (2019) Concomitant and controlled release  
577 of furazolidone and bismuth(III) incorporated in a cross-linked sodium alginate-  
578 carboxymethyl cellulose hydrogel. Int J Biol Macromol 126:359–366.  
579 <https://doi.org/10.1016/j.ijbiomac.2018.12.136>
- 580 Simonescu CM, Mason TJ, Călinescu I, et al (2020) Ultrasound assisted preparation of calcium  
581 alginate beads to improve absorption of Pb+2 from water. Ultrason Sonochem  
582 68:105191. <https://doi.org/10.1016/j.ultsonch.2020.105191>
- 583 Umamaheswari C, Lakshmanan A, Nagarajan NS (2018) Green synthesis, characterization and  
584 catalytic degradation studies of gold nanoparticles against congo red and methyl orange. J  
585 Photochem Photobiol B 178:33–39. <https://doi.org/10.1016/j.jphotobiol.2017.10.017>
- 586 Wang H, Shen J, Li Y, et al (2013) Porous Carbon Protected Magnetite and Silver Hybrid  
587 Nanoparticles: Morphological Control, Recyclable Catalysts, and Multicolor Cell  
588 Imaging. ACS Appl Mater Interfaces 5:9446–9453. <https://doi.org/10.1021/am4032532>

- 589 Xu K, Wu J, Fu Tan C, et al (2017a) Ag–CuO–ZnO metal–semiconductor multiconcentric  
590 nanotubes for achieving superior and perdurable photodegradation. *Nanoscale* 9:11574–  
591 11583. <https://doi.org/10.1039/C7NR03279J>
- 592 Xu Q, Xie L, Diao H, et al (2017b) Antibacterial cotton fabric with enhanced durability prepared  
593 using silver nanoparticles and carboxymethyl chitosan. *Carbohydr Polym* 177:187–193.  
594 <https://doi.org/10.1016/j.carbpol.2017.08.129>
- 595 Zhang X, Zheng H, Jin S, et al (2021) Fe<sub>3</sub>Pt-Ag nanoparticles: A novel generic approach  
596 towards detection and reduction for Rhodamine B. *J Solid State Chem* 293:121802.  
597 <https://doi.org/10.1016/j.jssc.2020.121802>
- 598
- 599
- 600

## Figures

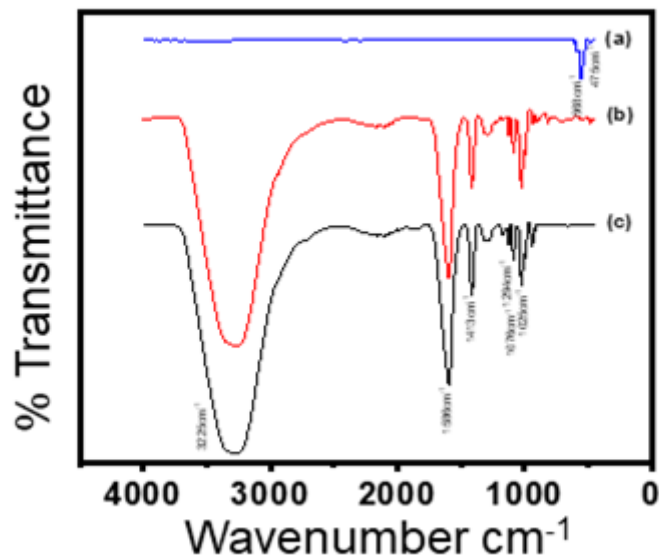


Figure 1

FTIR spectra for (a) Ag@NiO (b) Ag@NiO/Alg (c) pure Alg.

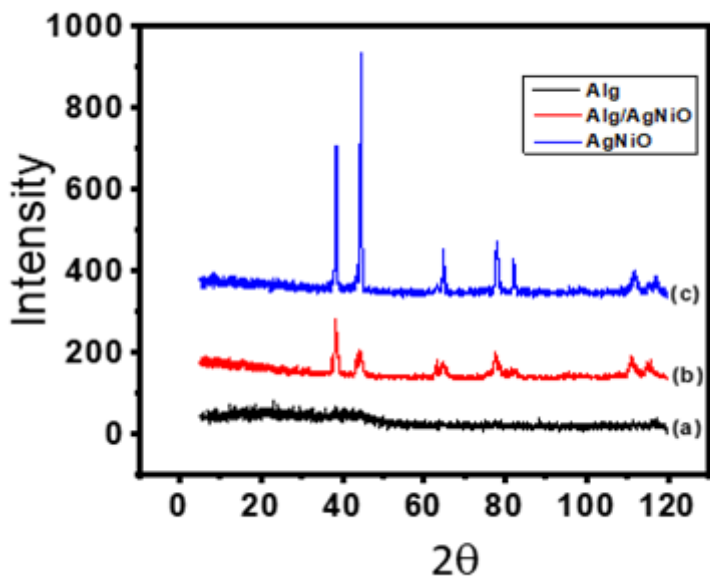
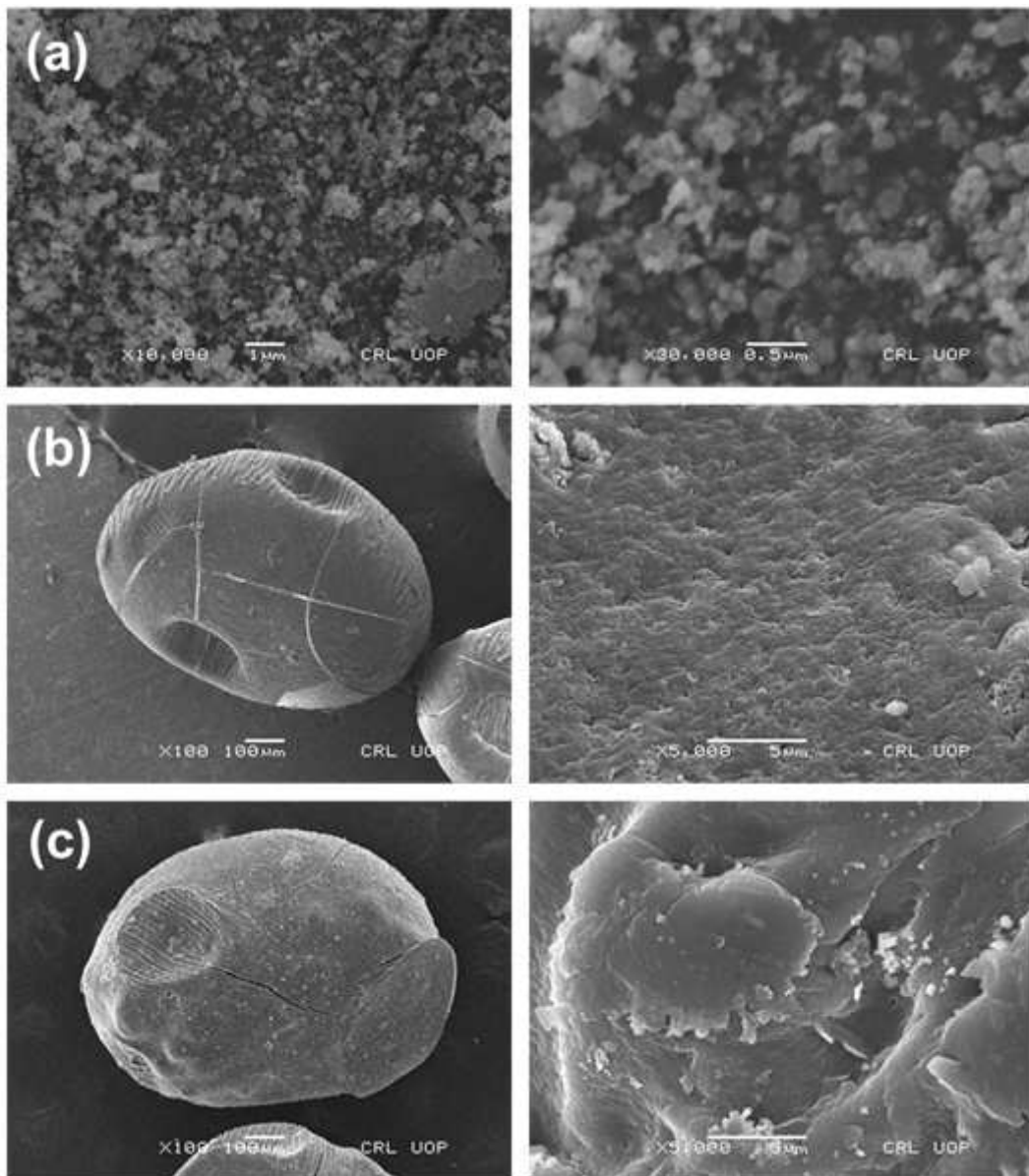


Figure 2

XRD pattern of (a) Alg beads (b) Ag@NiO/Alg beads (c) Ag@NiO nanoparticles.



**Figure 3**

SEM photographs of (a) Ag@NiO nanoparticles, (b) Alg beads and (c) Ag@NiO/Alg beads.

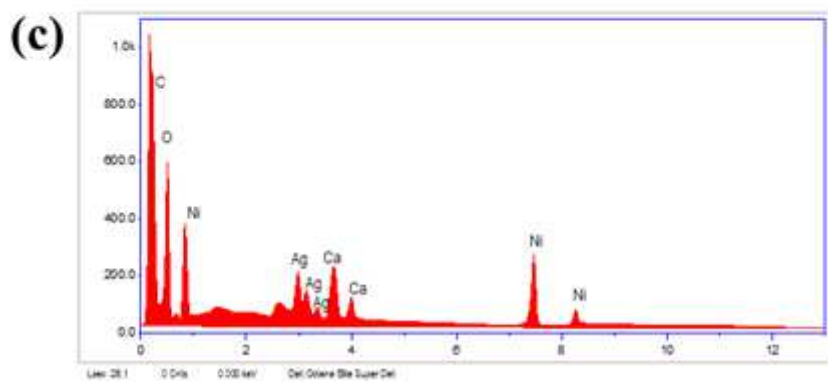
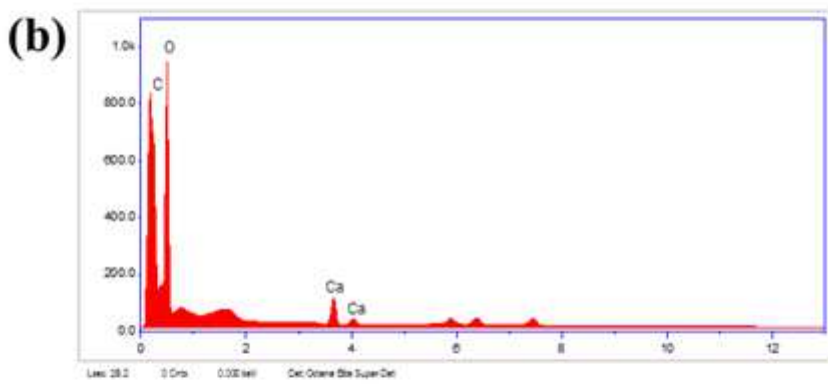
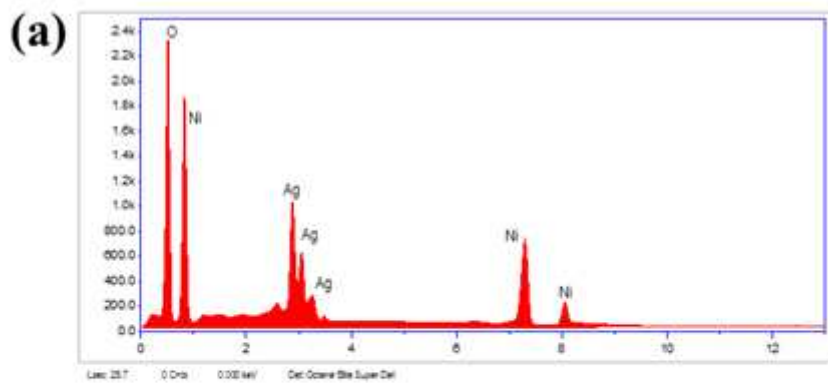


**Figure 4**

EDS spectral mapping for (a) Ag@NiO nanoparticles (b) Alg and (c) Ag@NiO/Alg beads.

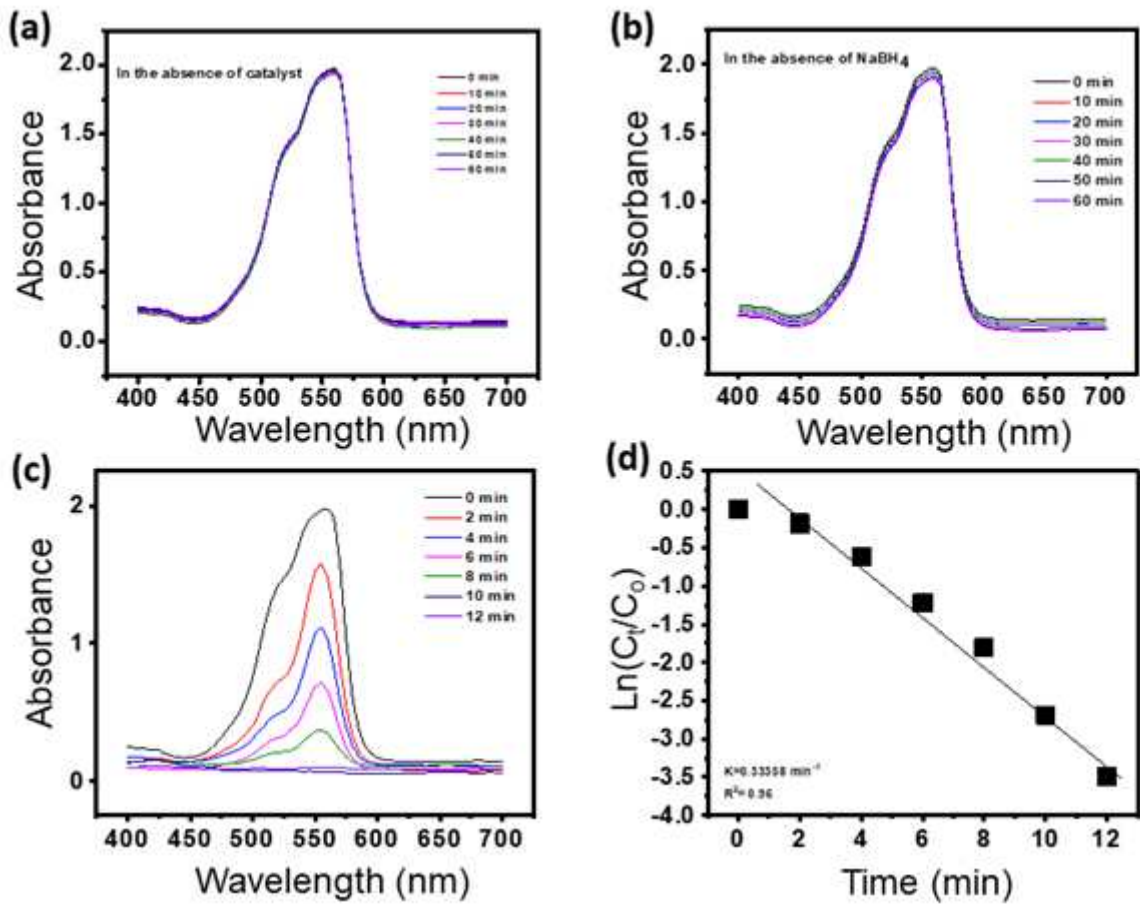


**Figure 5**

UV-Vis absorption spectra for 0.05mM RhB reduction (a) in the absence of catalyst with 0.1M NaBH<sub>4</sub> (b) in the absence of NaBH<sub>4</sub> with 0.1g of catalyst (c) in the presence of 0.1M NaBH<sub>4</sub> and 0.1g of catalyst (d) kinetic plot for reduction of 0.05mM RhB with 0.1M NaBH<sub>4</sub> as a reducing agent and 0.1g of catalyst

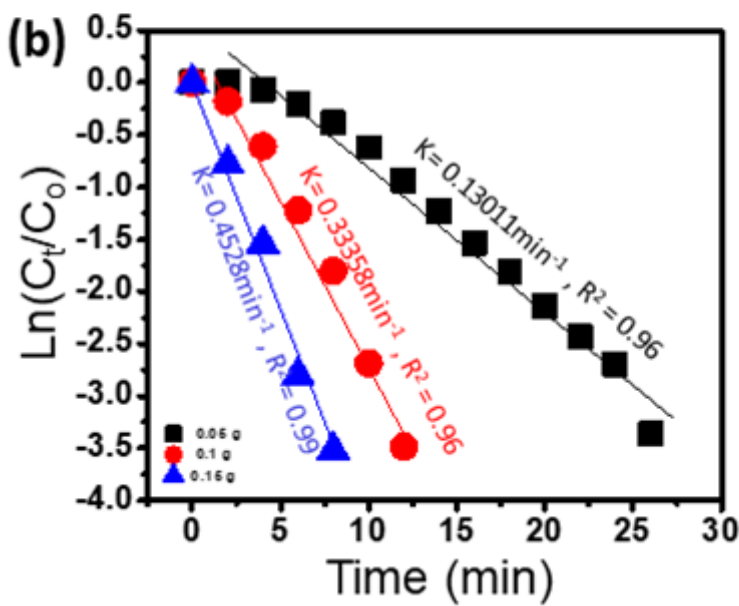
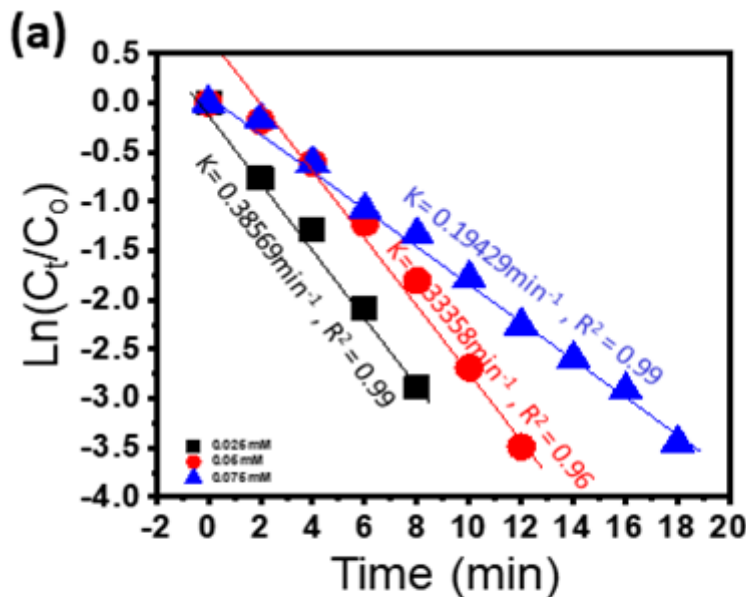


**Figure 6**

linear correlation of  $\ln C_t/C_0$  vs. time at (a) varying RhB concentration at 0.1M NaBH4 and 0.1g of catalyst and (b) varying catalyst dosage at 0.05mM RhB and 0.1M NaBH4

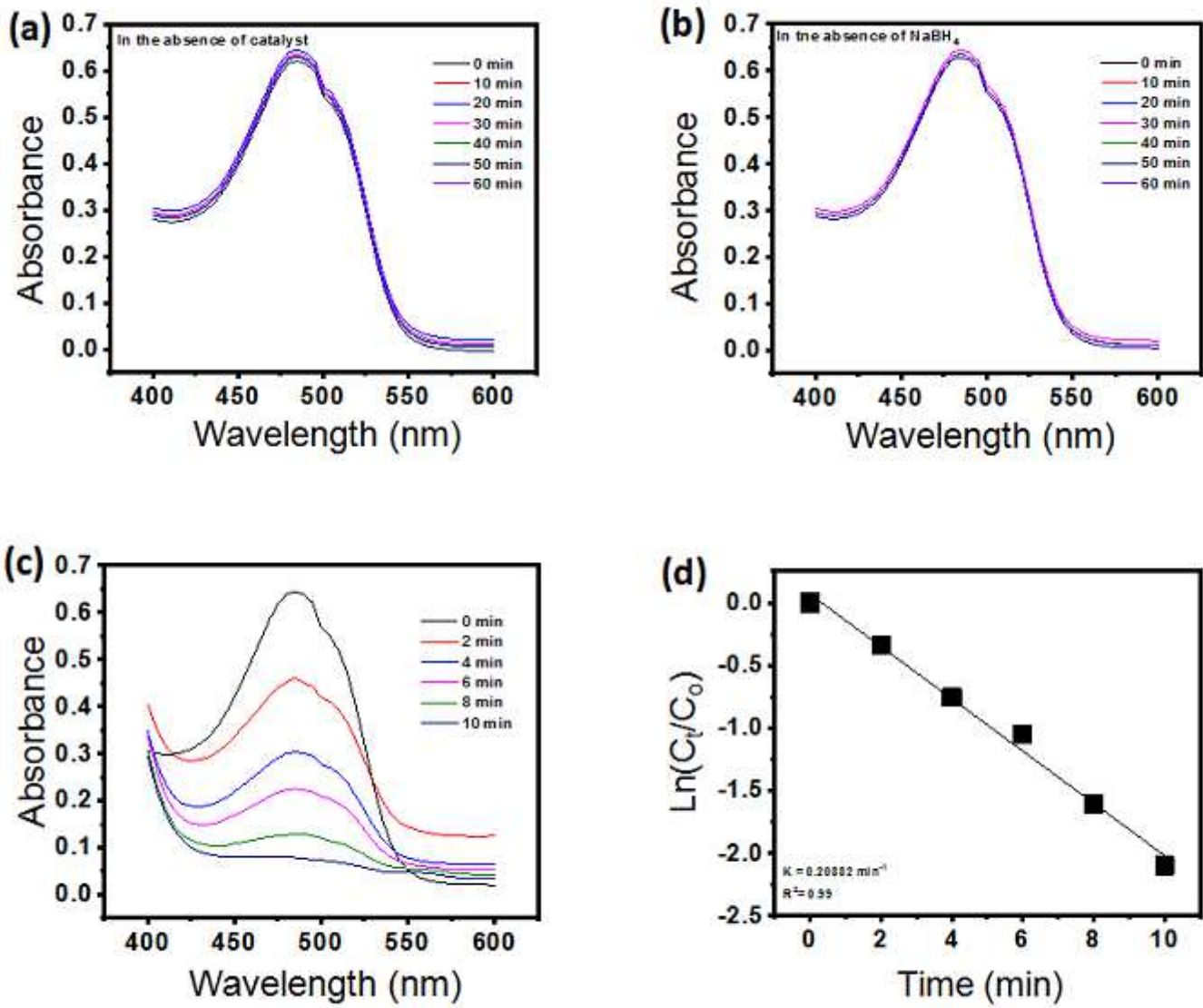


**Figure 7**

UV-Vis absorption spectra for 0.1mM MO reduction (a) in the absence of catalyst with 0.1M NaBH<sub>4</sub> (b) in the absence of NaBH<sub>4</sub> with 0.1g of catalyst (c) in the presence of 0.1M NaBH<sub>4</sub> and 0.1g of catalyst (d) kinetic plot for reduction of 0.1mM MO with 0.1M NaBH<sub>4</sub> as a reducing agent and 0.1g of catalyst.

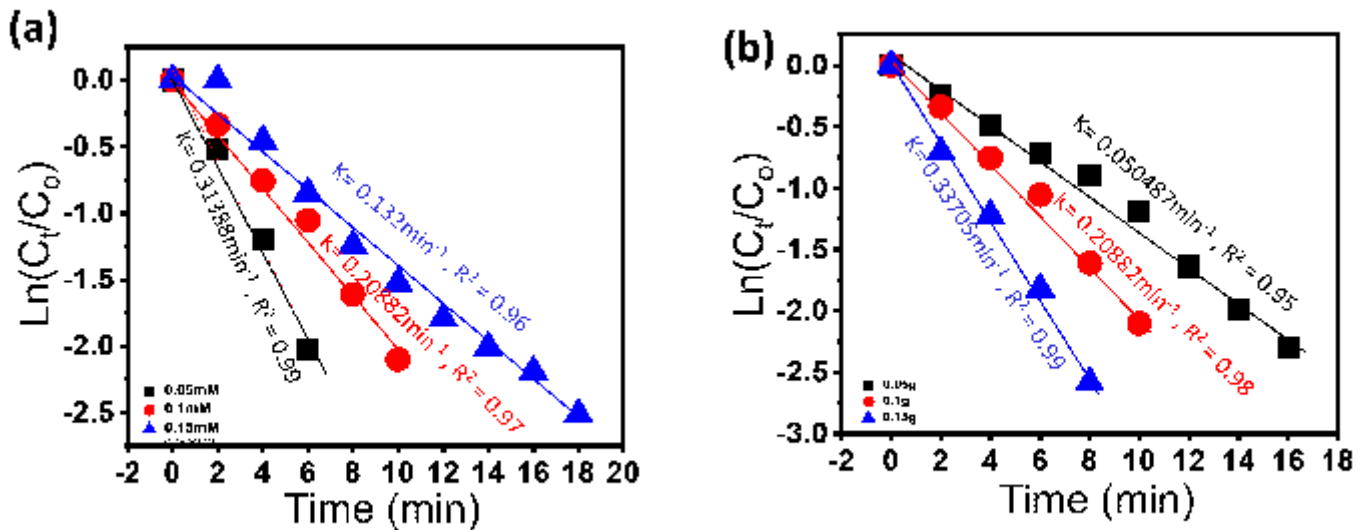


**Figure 8**

Linear correlation of  $\ln C_t/C_0$  vs. time at (a) varying MO concentration at 0.1M NaBH<sub>4</sub> and 0.1g of catalyst and (b) varying catalyst dosage at 0.1mM MO and 0.1M NaBH<sub>4</sub>

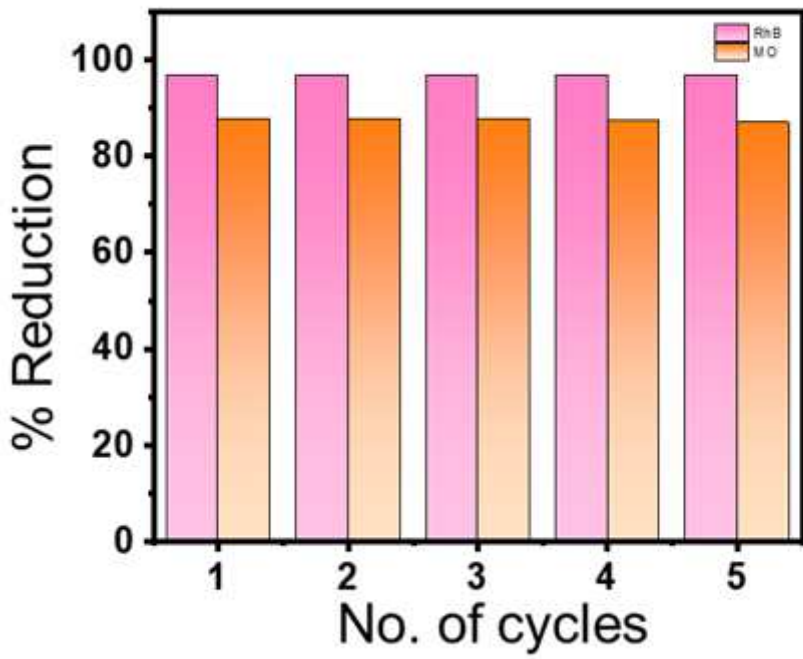


**Figure 9**

Reusability test results of Ag@NiO/Alg beads.

## Supplementary Files

This is a list of supplementary files associated with this preprint. Click to download.

- [GA.png](#)
- [Scheme01.png](#)